

AFOSR-TR- 82-0310

Edward L. Ginzton Laboratory  
W.W. Hansen Laboratories of Physics  
Stanford University  
Stanford, California

14

ACOUSTIC MICROSCOPY FOR NONDESTRUCTIVE EVALUATION  
OF MATERIALS

Final Report

for the period

1 July 1978 - 31 December 1981

Sponsored by  
Advanced Research Projects Agency (DOD)  
ARPA Order No. 3569  
Monitored by NE Under Contract #F49620-78-C-0098

The views and conclusions contained in this document are those of the authors and should not be interpreted as necessarily representing the official policies, either expressed or implied, of the Defense Advanced Research Projects Agency or the U.S. Government.

DTIC  
ELECTE  
S APR 26 1982 D  
D

Principal Investigator: Professor C.F. Quate

G.L. Report No. 3365

December 1981

Approved for public release;  
distribution unlimited.

82 04 26 044

AD A113874

DTIC FILE COPY

UNCLASSIFIED

SECURITY CLASSIFICATION OF THIS PAGE (When Data Entered)

REPORT DOCUMENTATION PAGE		READ INSTRUCTIONS BEFORE COMPLETING FORM
1. REPORT NUMBER <b>AFOSR-TR- 82-0310</b>	2. GOVT ACCESSION NO. <b>AD-A113 874</b>	3. RECIPIENT'S CATALOG NUMBER
4. TITLE (and Subtitle) <b>ACOUSTIC MICROSCOPY FOR NONDESTRUCTIVE EVALUATION OF MATERIALS</b>		5. TYPE OF REPORT & PERIOD COVERED <b>Final Report 1 July 1978-31 December 1981</b>
7. AUTHOR(s) <b>C.F. Quate</b>		6. PERFORMING ORG. REPORT NUMBER <b>G.L. Report No. 3365</b>
9. PERFORMING ORGANIZATION NAME AND ADDRESS <b>Edward L. Ginzton Laboratory Stanford University Stanford, California 94305</b>		8. CONTRACT OR GRANT NUMBER(s) <b>F49620-78-C-0098</b>
11. CONTROLLING OFFICE NAME AND ADDRESS <b>Advanced Research Projects Agency 1400 Wilson Boulevard Arlington, Virginia 20332</b>		10. PROGRAM ELEMENT, PROJECT, TASK AREA & WORK UNIT NUMBERS <b>ARPA Order 3569 Program Code 8Y10</b>
14. MONITORING AGENCY NAME & ADDRESS (if different from Controlling Office) <b>Air Force Office of Scientific Research Building 410 Bolling AFB, DC 20332</b>		12. REPORT DATE <b>December 1981</b>
		13. NUMBER OF PAGES <b>81</b>
		15. SECURITY CLASS. (of this report) <b>UNCLASSIFIED</b>
		15a. DECLASSIFICATION/DOWNGRADING SCHEDULE
16. DISTRIBUTION STATEMENT (of this Report)  <b>"Approved for public release; distribution unlimited"</b>		
17. DISTRIBUTION STATEMENT (of the abstract entered in Block 20, if different from Report)		
18. SUPPLEMENTARY NOTES		
19. KEY WORDS (Continue on reverse side if necessary and identify by block number) <b>Acoustics,                      Imaging,                      Integrated Circuits Materials,                      Photoacoustics, Microscopy,                      Nondestructive Evaluation (NDE),</b>		
20. ABSTRACT (Continue on reverse side if necessary and identify by block number) <b>This report covers the results of a research program on Acoustic Microscopy directed toward the study of integrated circuits and solid materials. This new type of microscopy permits one to examine microscopic features that are inaccessible in the optical microscope. Thus detail beneath metallization layers as well as the grain boundaries in polished samples can be examined without resorting to chemical etching. Adhesion of thin film is a field where acoustic microscopy will play an important role. Photoacoustic imaging is emerging as a key element in the study of thermal properties of materials</b>		

DD FORM 1 JAN 73 1473 EDITION OF 1 NOV 65 IS OBSOLETE  
S/N 0102 LF 14-6601

UNCLASSIFIED

SECURITY CLASSIFICATION OF THIS PAGE (When Data Entered)

UNCLASSIFIED

SECURITY CLASSIFICATION OF THIS PAGE(When Data Entered)

20. (continued)

and some initial results in this area are included.

Accession For	
NTIS GRA&I	<input checked="" type="checkbox"/>
DTIC TAB	<input type="checkbox"/>
Unannounced	<input type="checkbox"/>
Justification	
By	
Distribution/	
Availability Codes	
Dist	Avail and/or Special
A	



UNCLASSIFIED

SECURITY CLASSIFICATION OF THIS PAGE

## SECTION I

### INTRODUCTION TO ACOUSTIC AND PHOTOACOUSTIC MICROSCOPY

This is a final report on the work that has been carried out in the field of acoustic microscopy as a new method for studying the microscopic details of materials and fabricated microcircuits. The progress that came about with the support that was furnished under this program has enabled us to demonstrate an instrument that is capable of resolving structures that were heretofore imaging in the optical microscope. The properties of this instrument are such that certain elastic properties of the specimen under observation can be imaged in a way that is unique. The new instrument has proved attractive to those who produce commercial microscopes of the conventional type. By the end of 1982 we expect to see on the market prototypes of commercial instruments which derive directly from the work as carried out in the Ginzton Laboratory.

This report also marks the beginning of a new form of imaging which is termed photoacoustic imaging. It is responsive to the heating produced by the absorption of light from an intense laser beam.

Much of what we include here has been reported in previous reports on this program and the latest of these is the Annual report (G.L. 3295) of July 1981.

The acoustic reflection microscope is reviewed and its operation at higher frequencies is discussed. Imaging at frequencies as high as 3.6 GHz is reported. To accomplish this, a new type of transducer was developed, and acoustic lenses as small as 16 microns radius were employed. Noise and interference in high resolution acoustic microscopy

are considered and some images are included (Sections 2 and 3).

In Section 3 we present results of materials studies with acoustic microscopy. In a series of metallurgical samples, composite materials, and layered structures, we find that the acoustic images yield useful information about the mechanical properties of these samples that is not readily available from other forms of microscopy.

Section 4 considers the problem of adhesion of a film to a substrate. This is a simple mechanical property about which other microscopic techniques offer little or no information. In a series of acoustic micrographs of films with good and poor adhesion, film adhesion is found to be a strong source of contrast in reflection acoustic microscopy. Acoustic imaging is thus proposed as a new and nondestructive technique for evaluation of film adhesion.

It has been known for a hundred years that a modulated light source absorbed by a sample produces sound. In Section 5 we introduce photoacoustic microscopy based on this principle. Early photoacoustic images are found to offer information available to optical microscopy. A detailed theory of photoacoustic generation is developed. A plane wave theory for two different geometries (two regions and three regions) predicts the image contrast to be expected in photoacoustic images.

AIR FORCE OFFICE OF SCIENTIFIC RESEARCH (AFSC)  
NOTICE OF TRANSMITTAL TO DTIC  
This technical report has been reviewed and is  
approved for public release IAW AFR 190-12.  
Distribution is unlimited.  
MATTHEW J. KERPER  
Chief, Technical Information Division

## SECTION 2

### HIGH FREQUENCY ACOUSTIC MICROSCOPY

#### 2.1 General Considerations

The acoustic microscope<sup>1,2,3</sup> has produced images with sound waves at frequencies from tens of MHz to over 3 GHz. To achieve the highest resolution, we use the highest practical frequency. In this chapter we consider the extension of the operating frequency of the microscope to 3.6 GHz. A new transducer structure was developed to achieve this, which reduces interference between pulses for imaging with very small lenses. We begin by reviewing acoustic microscope operation and general imaging considerations. Sources of noise and interference are considered in detail. We close with discussion of the 'flat' pulse, a remaining problem of very small acoustic lenses.

The acoustic microscope reveals information about the mechanical properties of small objects. This information is complementary to the information revealed about the same objects by optical microscopes or electron microscopes. A number we wish to know about any microscope is its resolution. That is, the smallest distance between objects revealed in our microscope as being separate objects rather than one extended blur.

The fundamental limitation on the resolution of any microscope is the wavelength used for imaging. The highest spatial frequency transmitted by an imaging system employing wavelength  $\lambda$  is:

$$v_0 = \frac{2(N.A.)}{\lambda} = \frac{1}{\lambda(f\#)} \quad (2.1)$$

where N.A. = numerical aperture and  $f\#$  = focal length/lens aperture diameter.<sup>4</sup>

Taking the reciprocal of this frequency as a useful definition of resolution thus gives

$$s_{\min} = \lambda(f\#) \quad (2.2)$$

This corresponds to the wavelength of the highest spatial-frequency variation in image contrast which the imaging system passes.

The Rayleigh criterion, based on setting the maximum of the circular diffraction pattern of a point on top of the first minimum of the diffraction pattern of an adjacent point, finds these points barely resolved with spacing:<sup>5</sup>

$$s_{\min} = \frac{.61\lambda}{(N.A.)} = 1.22 \lambda(f\#) \quad (2.3)$$

For a sapphire acoustic lens with half-opening angle  $50^\circ$  operating in water, we have

$$f\# = \frac{1.15 r}{2r \sin 50^\circ} = .75$$

The spatial frequency criterion and Rayleigh criterion give  $.75\lambda$  and  $.92\lambda$ , respectively, for the point resolution of the microscope.

We are driven in a search for greater resolution to smaller wavelengths. Since  $\lambda = v/f$  for any wave, where  $v$  = wave velocity and  $f$  = frequency, one can decrease  $\lambda$  by decreasing  $v$  or increasing  $f$ .

For the acoustic microscope, wave velocity  $v$  is determined by the choice of fluid. This is, in turn, influenced by convenience and the attenuation constant  $\alpha$ , where

$$I = I_0 e^{-2\alpha z} \quad (2.4)$$

gives the intensity of sound in a plane wave after propagation through distance  $z$ . For many fluids,

$$\frac{\alpha}{f^2} = \text{constant} \quad (2.5)$$

and thus as one moves to higher frequencies to gain in resolution, the attenuation of sound increases rapidly.

Attal and Quate<sup>6</sup> have measured attenuation constants  $\alpha$  and have ranked fluids on the basis of a figure of merit whose definition depends on the type of attenuation observed. The most interesting of the available liquids for acoustic microscopy are listed in Table 2.1. Acetone and benzene are included to illustrate that organic liquids typically have attenuation substantially higher than water and are thus not useful for high-resolution microscopy. Methanol actually has a higher figure of merit than room temperature water and may prove useful in photo-acoustic microscopy, due to its high expansion coefficient. This topic will be considered in Section 5.



TABLE 2.1  
Figure of Merit for Various Liquids<sup>9,11</sup>

Liquid	Temperature	Velocity (km/sec)	$\alpha/f^2$ ( $\times 10^{17}$ sec <sup>2</sup> /cm)	Impedance ( $\times 10^{-5}$ gm/cm <sup>2</sup> -sec)	F.M.
water	25°C	1.495	22.0	1.495	1.0
water	37°C	1.523	17.7	1.523	1.10
water	60°C	1.55	10.2	1.55	1.42
Methanol	30°C	1.088	30.2	0.866	1.13
Acetone	30°C	1.116	54.2	0.916	0.80
Benzene	25°C	1.310	873.0	1.15	0.17
Carbon disulfide	25°C	1.310	10.1	1.65	1.70
Mercury	23.8°C	1.449	5.8	19.69	2.01
Gallium	30°C	2.87	1.58	17.48	1.66
Nitrogen	77°K	0.85	12.9	0.68	2.2
Argon	87°K	0.84	14.1	1.2	2.2
Helium	4.22°K	0.183	260.0	0.027	2.70
Helium	0.45°K	0.238	5.8	0.035	13.81

The liquids Ga<sup>7</sup> and Hg<sup>8</sup> have been employed for imaging at room temperature. They are more difficult to handle, have wetting problems, and are incompatible with many samples.

The cryogenic liquids nitrogen, argon, and 4K helium have all been used for imaging, the former two more often to date than helium, due to the latter's extremely low impedance and the consequent difficulty in coupling sound out of a lens into liquid He. At the present time intensive work continues on liquid He at ~ 200 mK.<sup>9</sup>

## 2.1 High Frequency Water Microscopy

In the present work the high frequency operation of the acoustic microscope in heated water is considered. Water, due to its universal availability, safety, ease in handling, and compatibility with most samples, is highly attractive and fortunately has low acoustic attenuation for a near-room temperature liquid when it is heated. Water's velocity and attenuation constant are shown in Fig. 2-1. Keeping in mind that small wavelength desirable for high resolution requires low attenuation or low velocity, one sees from the figure that one must accept a small increase in velocity (~10%) to gain a large decrease in acoustic attenuation which permits higher frequency operation. The best achievable resolution with water is with the hottest water practical: 60 - 90 C. All of the acoustic pictures to be shown used water in this temperature range.

Carbon disulfide, listed as having a higher figure of merit than water in Table 2.1, was also used for imaging at 2.7 GHz and 3.1 GHz. Although images were acceptable, signal-to-noise was in each case several decibels lower than in water at the same frequency. The real

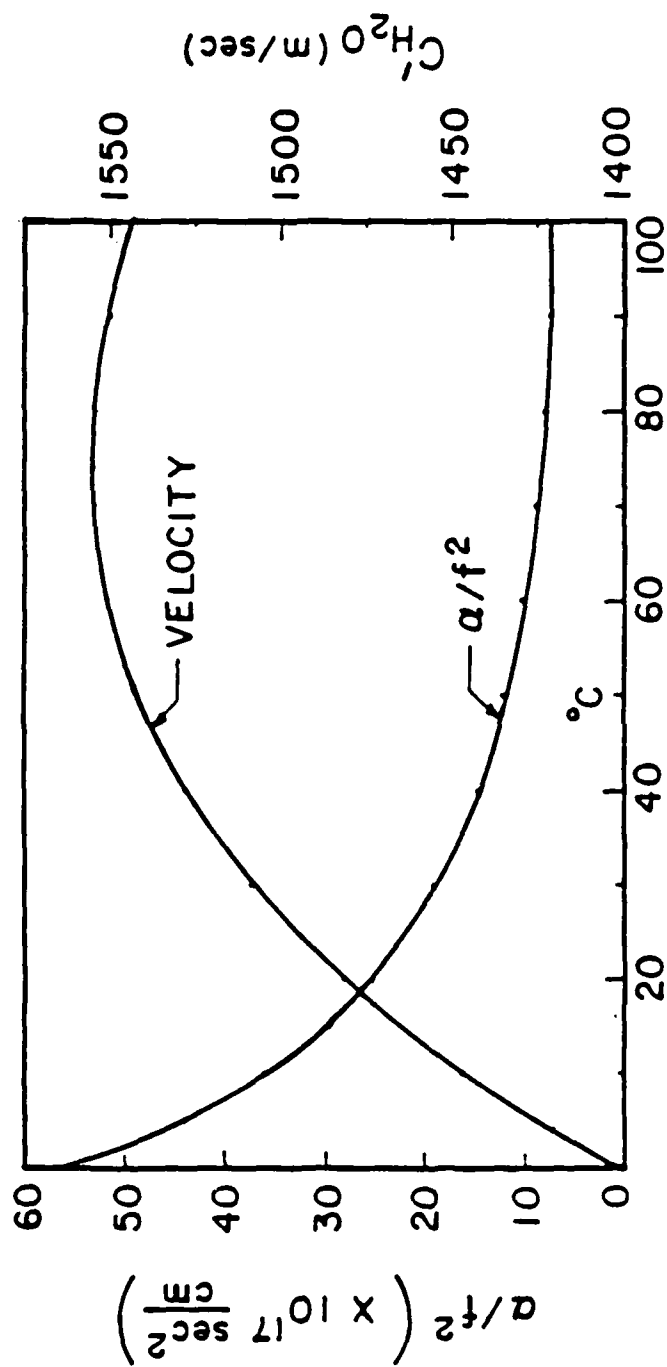


FIG. 2.1. Velocity and attenuation in water as a function of temperature.<sup>1</sup>

improvement promised by  $\text{CS}_2$ 's high figure of merit was not apparent. This conclusion was reached previously by Jipson.<sup>10</sup> Its volatility at room temperature and noxious character require a noticeable advantage over water for one to consider  $\text{CS}_2$ . One possible use for  $\text{CS}_2$  in acoustic microscopy is for samples harmed by water (iron, for example) where room temperature evaluation is required.

In Figs. 2-2 and 2-3 we show the essentials of the reflection microscope's operation. In Fig. 2-2 we have the acoustic lens, whose fabrication has been described elsewhere. Briefly, in Fig. 2-2, a short pulse of microwave energy is coupled to a ZnO thin-film transducer (B) by a matching network (A) consisting of a quarter-wavelength section of characteristic impedance  $10 \Omega$  fabricated on  $\epsilon - 10$  microwave substrate. Ten ohms is chosen as the geometric mean between the input transmission line  $50 \Omega$  and the approximately  $2 \Omega$  acoustic radiation resistance of the ZnO transducer and sapphire substrate. The geometrical capacitance of the transducer is resonated with the bond wire acting as a series inductance.

The input rf pulse excites a pulse of sound in the sapphire which propagates to the lens (C in Fig. 2-2) on the opposite end of the crystalline rod. The transducer size and location is selected with care to insure proper illumination of the lens. A quarter-wavelength thickness of sputtered glass acts as an anti-reflection coating to couple sound into the coupling fluid, usually heated water.

The spherical shape of the lens gives negligible spherical aberration at the focus of the lens, due to the large 7.15/1.0 velocity ratio of sapphire to water.<sup>11</sup>

The sample (D in Fig. 2-2) reflects the sound with a reflectance function depending on its material properties. The pulse is recombined into a beam by the lens, and excites an electrical signal at the transducer. This signal, separated in time from other reflections in the system is routed by the circulator to the receiver electronics.

The system diagram of the microscope is shown in Fig. 2-3. On the receiver side of the circulator, a PIN absorption switch is used as a time gate to pass the pulse representing information reflected back from the sample while suppressing other signals.

The amplified, reflected pulse from the sample is sampled and held after detection and pulse amplification. Its magnitude is used to modulate the brightness of the CRT display.

The image is produced by mechanically scanning the sample at 20 - 60 Hz in the x direction while a DC motor raises the sample in the y direction, generating a raster pattern requiring ~ 15 sec for 1 frame. The basic pulse repetition rate is 300 kHz producing ~ 1000 pulses per scan line on the display, or ~ 1 pulse/resolution element, when the fast scan frequency is 60 Hz. This changes to ~ 3 pulses/resolution element at 20 Hz. The sample position is sensed and used to position the CRT spot. The image is first written at the 15 sec/frame rate onto a scan converter, which then writes the image to the high resolution television monitor at 30 frames/second in TV format. The image is then photographed from the television monitor.

Special care must be given to certain aspects of the system in Figs. 2-2, 2-3 for high frequency operation. In Fig. 2-3, the RF

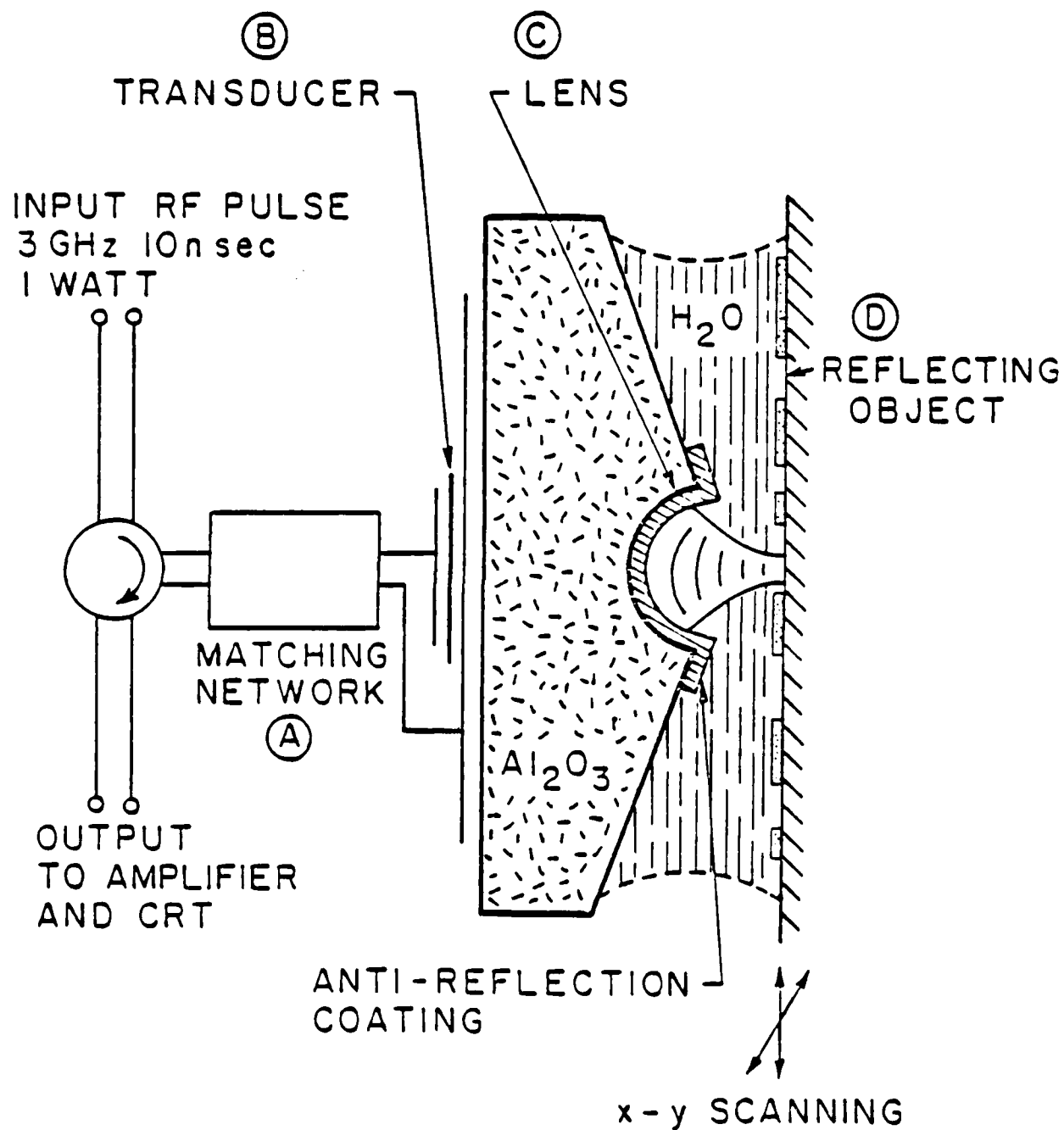


FIG. 2-2. The acoustic lens.

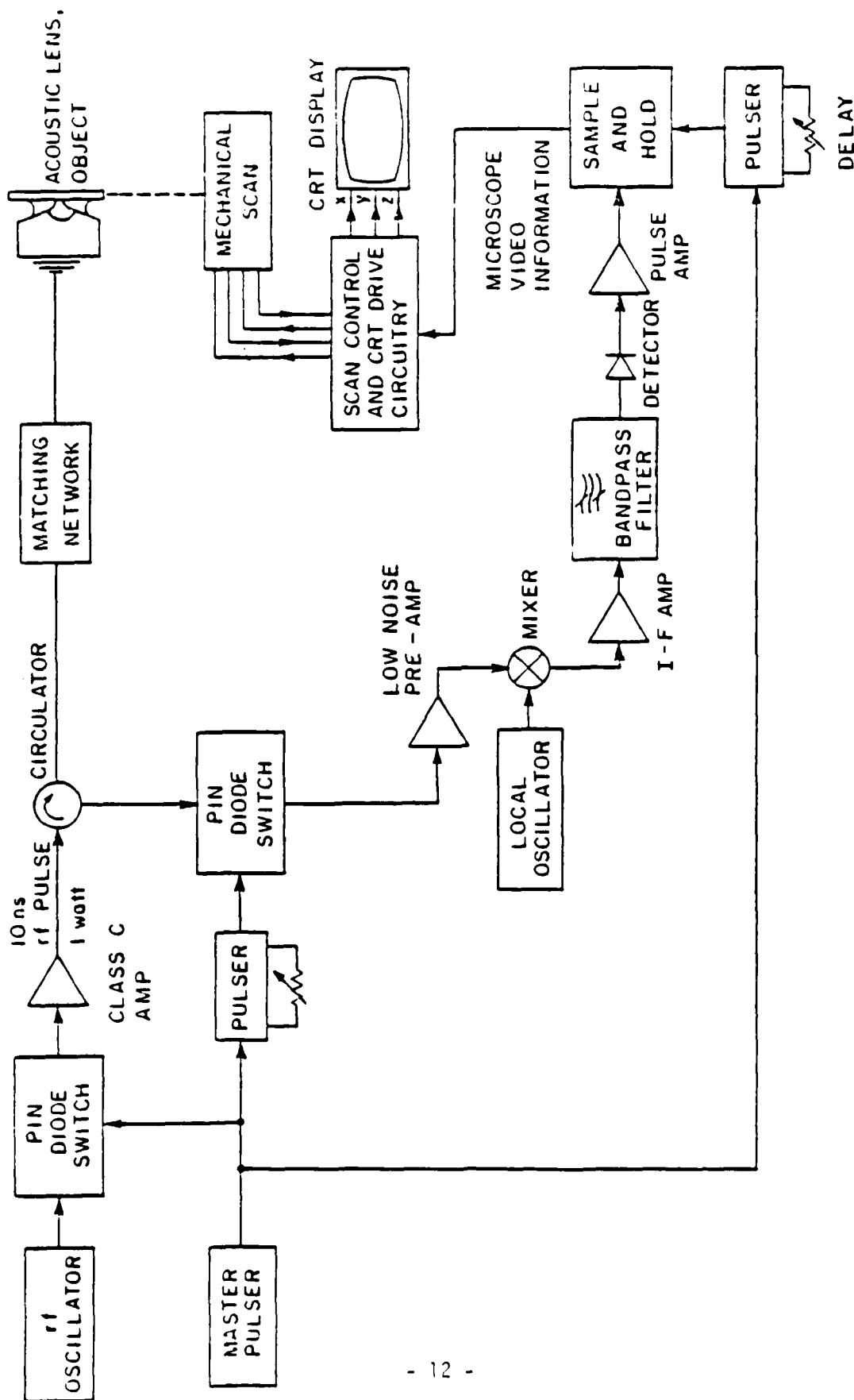


Fig. 2-3. Reflection acoustic microscope system diagram.

pulse must be exceptionally clean and hence a class C amplifier was designed and built using microstrip matching networks and an NEC 3001 microwave transistor in common-base arrangement. This amplifier was measured to have 9 dB of gain in the bandwidth 2.7 - 3.0 GHz with an output power at peak of 1.6 watt for a 10 nsec pulse. As we will discuss shortly, the input RF pulse must have an exceptionally sharp fall to avoid interference with the signal reflected from the sample, and this was the function of the class C amplifier.

### 2.3 Noise Considerations and Lens Design

To achieve reasonable signal-to-noise ratio with high acoustic frequencies in the acoustic microscope we must operate with small lenses to minimize the acoustic loss in water. To treat this quantitatively, let us follow a typical acoustic pulse through the system. We assume an input rf pulse peak power level of 30 dBm = 1 watt. At 3 GHz, and above, typical two-way ZnO transducer insertion loss is 20 dB. There is two-way illumination loss of typically 10 dB in that not all power emitted by the transducer strikes the lens. The matching layer on the front of the lens has loss typically 1 dB one way, 2 dB two ways. Adding these losses and assuming a perfect reflector at the focus gives a reflected signal at the output of -2 dBm in the absence of acoustic attenuation.

Assuming cleanly falling pulses and sufficient isolation by the rf switches, the lower limit on detectable signals is the thermal noise power level:

$$P_n = kT\Delta f$$



where  $k$  = Boltzmann's constant;  $T$  = absolute temperature;  $\Delta f$  = system noise bandwidth. The noise bandwidth  $\Delta f$  must be considered carefully. In our sample and hold system, in the absence of signal averaging (which we would have if we ran many pulses per resolution element), the signal/noise ratio is frozen in by the sampling process. This may be modeled as a switch periodically opening and closing to allow a capacitor  $C$  to charge to the voltage at the output of the detector when the switch is closed (coinciding with the arrival of a signal pulse at the detector output). See Fig. 2-4. The charging time constant  $RC$  is assumed small relative to the time the switch is closed. The voltage held by the sampling capacitor represents detected signal plus noise power. The signal/noise ratio is not changed further by amplifier  $A_2$ , which is typically configured as a low pass filter. We should emphasize again our assumption that we are using one pulse per resolution element.

The sampling capacitor has an  $RC$  time constant chosen to be smaller than the time the switch is closed, allowing the storage capacitor to reach essentially full charge. As an  $RC$  circuit it also acts as a low pass filter, having a cutoff given by

$$\Delta f_s = \frac{1}{2\pi RC}$$

This bandwidth is approximately equal to the IF bandwidth  $\Delta f_1$  in our system, because the time  $RC$  was chosen to be a fraction of the aperture time when the switch was closed. As an example:  $R = 50\Omega$ ; Typical  $C = 30$  pF gives  $RC = 1.5$  nsec ;  $\Delta f_s = 106$  MHz . In our system the IF bandwidth is chosen as the reciprocal pulse length, or 100 MHz for a 10 nsec pulse.

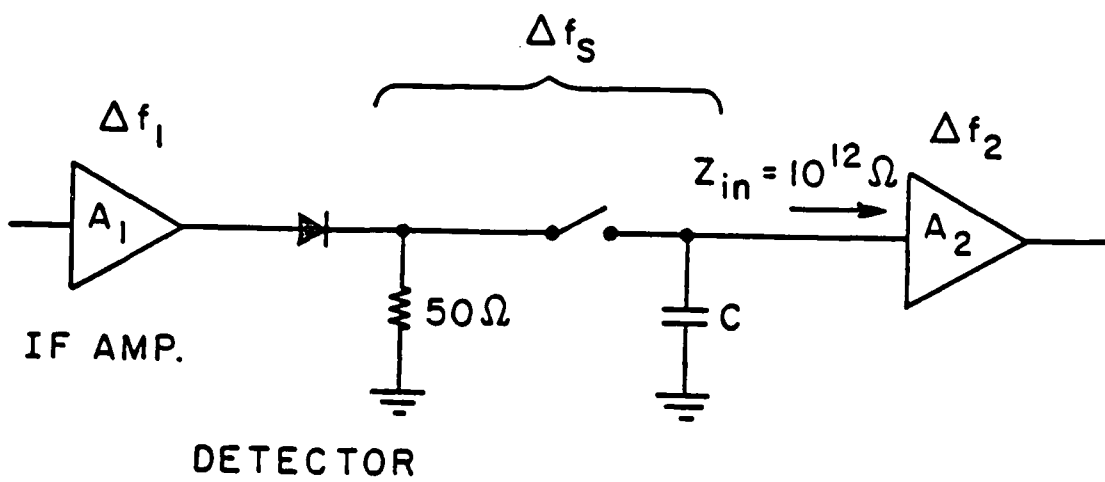


FIG. 2.4 Sample and hold system.

We want the overall noise bandwidth for a system as shown in Fig. 2-4, with the switch closed and neglecting amplifier  $A_2$ . This is an IF amplifier of noise bandwidth  $\Delta f_1$  driving a square-law detector, followed by a low-pass filter with bandwidth  $\Delta f_s$ . When  $\Delta f_s \sim \Delta f_1$  overall noise bandwidth can be shown to be:<sup>12</sup>

$$\Delta f_n = 2\Delta f_1$$

If one does signal averaging by allowing  $N$  pulses per resolution element, this effective overall noise bandwidth is reduced as  $\sqrt{N}$ , since the signal content of each pulse is presumed to remain constant while the noise is random.

Thus a useful approximate expression for the overall thermal noise power in the sampled-and-held system we describe is:

$$P_n = \frac{2kT \Delta f_1}{\sqrt{N}}$$

where  $N$  is the number of pulses per resolution element, and  $\Delta f_1$  is the IF bandwidth. The thermal noise power in a system with 100 MHz IF bandwidth and  $N = 1$  is readily found to be -91 dBm.

With no acoustic attenuation we found -2 dBm transducer output signal level typical for a 1 watt input pulse and a perfect reflector. This is 89 dB above the thermal noise level. Assuming a system noise figure of 5 dB, this leaves 84 dB as the sum of the signal-to-noise ratio of our signal and the water attenuation. Thus with signal/noise = 25 dB we can tolerate 59 dB of water loss, and with signal/noise = 40 dB we can tolerate 44 dB of loss.

From these numbers it is a simple matter to calculate lens size needed for a given signal/noise ratio. In Table 2.2 are shown lens sizes for two different signal/noise ratios at two different water temperatures. The first column, with 44 dB calculated water loss, 40 dB calculated signal/noise, is certainly a more practical and realistic set of numbers for reliable lens design. As we shall see in Section 3, 4, and 5, many of the most interesting acoustic micrographs (for the information they reveal about a sample) are taken at out-of-focus lens positions where signals are 20 dB or more below the level one expects for a perfect reflector in the focal plane. It is desirable to have 25 dB of signal/noise ratio at these out-of-focus positions, which means designing for 40 dB or more signal/noise in focus.

#### 2.4 Pulse Separation and Transducer Design

As lens sizes are made smaller, separation of pulses within the system becomes more difficult. In Fig. 2-5 we see the acoustic lens with an input pulse of 10 nsec width, 1 watt peak power. This pulse passes from the circulator to the transducer at a. Although there is a matching network (not shown) between circulator and transducer, inevitable mismatch produces the output reflection a as shown. This pulse is typically 10 dB down from the input. The transducer produces a pulse of sound which propagates from a to the lens at b in the figure. There is inevitable mismatch at the lens for sound to couple into water, and hence the reflected acoustic pulse excites the transducer and emerges as an RF pulse b, at a time equal to one round trip time in the sapphire, which is 360 nsec for the 2 mm rod shown. This pulse is typically 30 dB below the level of pulse a. There is a

TABLE 2.2  
 Lens Size for Given Signal-to-Noise Ratio  
 at Two Water Temperatures

f	$\lambda_{H_2O}$	$r_{40dB, 60C}$	$r_{25dB, 80C}$
1.0 GHz	1.55 $\mu$	216 $\mu$	336 $\mu$
1.5 GHz	1.03 $\mu$	96 $\mu$	149 $\mu$
2.0 GHz	775 nm	54 $\mu$	84 $\mu$
2.5 GHz	620 nm	35 $\mu$	54 $\mu$
3.0 GHz	517 nm	24 $\mu$	37 $\mu$
3.5 GHz	442 nm	18 $\mu$	27 $\mu$
4.0 GHz	388 nm	13 $\mu$	21 $\mu$

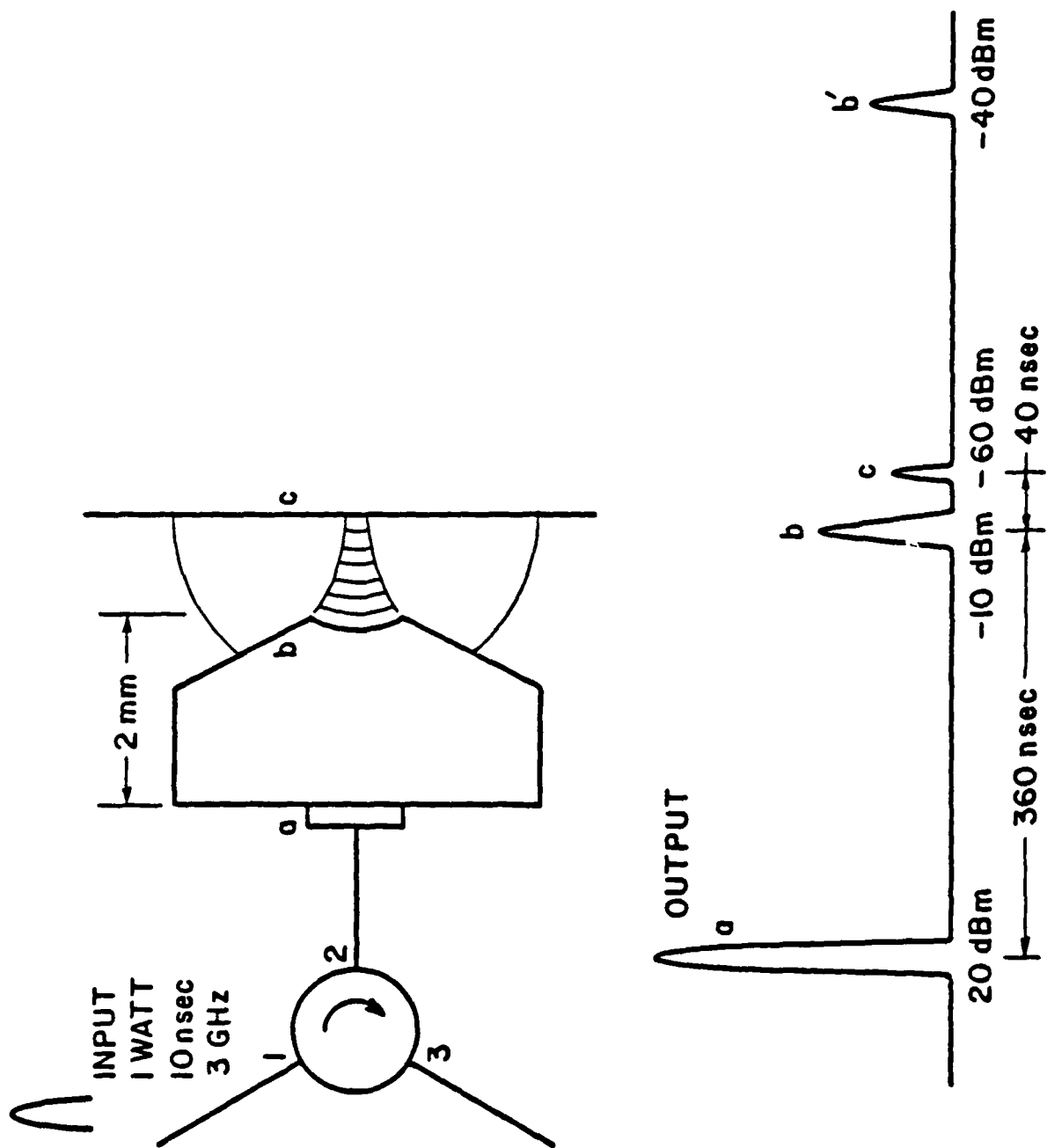


FIG. 2.5. Output pulses in the reflection acoustic microscope.

second pulse after two round trips at  $b'$ , and echoing continues until the echoes are lost in thermal noise. This echoing sets an upper limit of about 1 MHz on the pulse repetition rate, because it is most undesirable for echoes of a previous pulse to be present in the system where they could interfere with the return from the sample.

The return from the sample is labeled  $c$  in Fig. 2-5 and occurs after pulse  $b$  by a time equal to one round trip time from lens to sample through the water. Forty nanoseconds is the time for a  $27\mu$  radius lens, which is halved to 20 nsec for a  $13\mu$  lens. The inescapable fact for high frequency microscope performance is that the pulse  $b$  is typically 50 dB higher than pulse  $c$  occurring one round trip time in water later. Pulse  $b$  (as well as pulses  $a$  and  $b'$ ) is time-gated out of the system, but pulse  $b$  must have an exceptionally clean falling edge. To be in the noise, and not acting as interference with information pulse  $c$ , pulse  $b$  as shown would have to be 81 dB below its peak value 40 nsec after the peak.

To accomplish this one shapes the original incoming rf pulse with two PIN switches in series followed by a class C amplifier. They were found to produce a pulse 80 dB down from its peak 20 nsec after the peak.

A series of 4 lenses with radii  $24 - 30\mu$  and 4 test flats (sapphire rods with a plane end face for transducer evaluation) were fabricated for operation at 3.0 GHz. It was found that all transducers had good two-way insertion loss: 18 - 20 dB as measured with the test flats. Reflected pulses from samples were observed to be 20 - 35 dB above the thermal noise level for the 4 lenses. However, for 3 of the 4 lenses

the trailing edge of pulse b was found to be 5 - 15 dB above the thermal noise floor at the time of arrival of water pulse c . This seriously degraded the image quality of these 3 lenses; 2 of the 3 lenses were unusable.

An interfering signal 20 dB below a desired signal is more harmful to image quality than a thermal noise level 20 dB below the same desired signal. Recall that the interfering signal adds to the desired signal coherently. As the phase difference between the desired and interfering signals moves through  $\pi$ , this corresponds to  $\lambda/4 = 1250 \text{ \AA}$  added distance between lens and object. If the signals have amplitudes  $A$  and  $0.1A$ , there is a difference in detected power of  $(1.1A)^2 / (.9A)^2 = 1.49$  or 1.7 dB. A noise signal adding incoherently to a desired signal would produce 0.17 dB difference in detected power at most, if it were likewise 20 dB below the desired signal.

The behavior of the four above-mentioned lenses forced one to the conclusion that the transducer itself was broadening the incoming RF pulse, since reflected acoustic pulse b of Fig. 2-5 was substantially wider than pulse a . Examination of the transducers of the four lenses under an optical microscope yielded a surprising correlation between mechanical properties of the transducer and the pulse broadening. In Fig. 2-6 we show details of the electrical connection to the transducer. In Fig. 2-6(a) we show a 1 mil or 2 mil wire making the connection between the incoming microstrip line and the transducer top electrode. In Fig. 2-6(b) the scale is expanded to show that actual contact is made with a small gold ball which is bonded to the gold or platinum top electrode by thermal compression. It was found that for the four lenses tested, there was a direct correlation between ball size and acoustic pulse



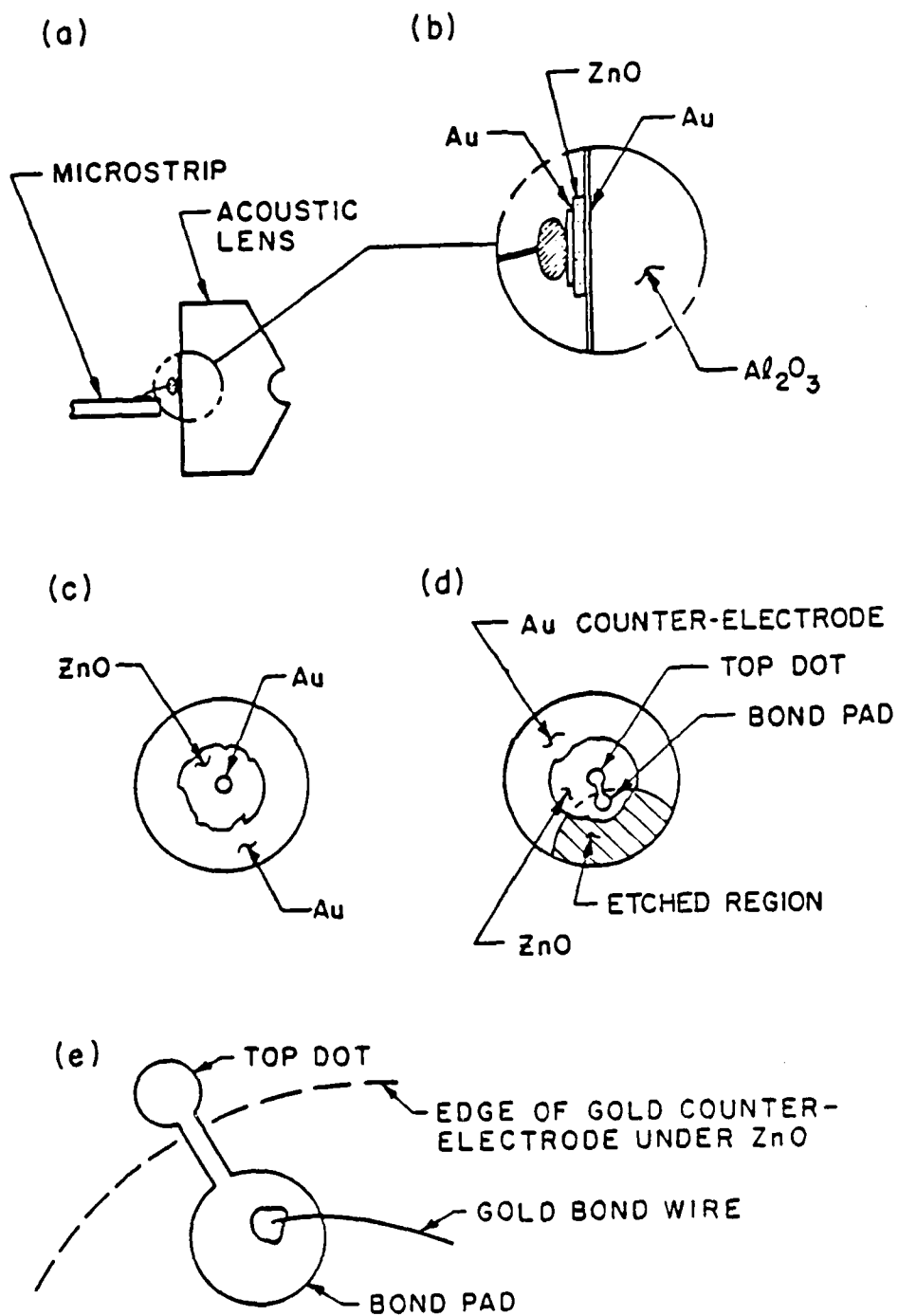


FIG. 2-6. Details of electrical connection to piezoelectric transducer.

broadening. In particular, the only really satisfactory lens of the four had by far the smallest ball, estimated to be  $\sim 50 \mu$  diameter, with up to  $\sim 120 \mu$  diameter for the others. The top electrode in the case of these 4 lenses was  $150 \mu$  diameter.

A hypothesis was formed that the ZnO transducer in Fig. 1-6(b) radiated sound into the gold ball on its back side as well as into the sapphire rod; that this sound wave, after reflection from the gold/air interface at the back of the ball, propagated into the sapphire; that when then reflected at the lens/water interface this sound appeared as a broadening of pulse b in Fig. 2-5.

To test this hypothesis, a series of 4 more lenses was fabricated with particular emphasis being laid to making the gold ball as small as possible. One mil diameter gold wire was used and the resultant gold ball diameter was estimated to average  $40 - 50 \mu$ . These lenses had noticeably less pulse broadening than did the prior group with no control over ball size. At 30 nsec after the peak, pulse b of Fig. -5 was typically 3 - 5 dB above the noise floor.

To attack the problem at its root, a new type of transducer structure was designed and fabricated in 4 test flats and 4 lenses. In Fig. 2-6(c) we show the traditional design transducer from the back side. A gold counter-electrode has been evaporated over the entire back surface of the lens as a ground plane. ZnO is rf sputtered over a large central area, and then a gold top electrode is defined by a liftoff procedure. The bond wire and gold ball are then affixed to the top electrode.

In Fig. 2-6(d) is an alternative design to remove the troublesome gold ball from the top electrode altogether. After the gold counter-electrode is laid down, a portion of it is etched away along a circular arc which passes to within  $\sim 10 \mu$  of the desired top electrode location. This location is located by etching a circular hole of the appropriate size in an  $\text{SiO}_2$  layer laid down prior to the gold counter-electrode deposition.<sup>13</sup> ZnO deposition is followed by top electrode definition, accomplished by liftoff of a gold layer evaporated over a photoresist layer removed at places where one wishes the gold to stick.

In this design the top electrode is a dumbbell-shaped region consisting of the transducer top electrode joined by a narrow ( $\sim 30 \mu$ ) strip to a circular bond pad which is laid down on the zinc oxide region having no remaining counter-electrode beneath it. See Fig. 2-6(e). Bonding is then accomplished by thermal compression of a gold ball to the bond pad.

The aim of this design was to stop spreading of the pulse by echos from the bond. It depends on the small region of the connecting strip that lies above the remaining counter-electrode having much smaller area than the circular top dot. Likewise, the capacitance to ground of the bond pad must be very much less than the capacitance of the top dot. Both of these assumptions must be valid or we expect a seriously distorted field pattern at the lens.

Transducers of this design were fabricated on lenses with radii 16 - 19  $\mu$  and test flats. These transducers had good 2-way insertion loss: 18 dB at 3.1 GHz and 18 dB at 3.4 GHz were measured in two different runs. They also were found to give substantially less

broadening of the pulse reflected from the lens/water interface. The falling edge of this pulse was found to be below the thermal noise level 30 nsec after the peak for 4 lenses, and in one case a level 65 dB below the peak 20 nsec after the peak was measured.

Work with these transducers to date indicates their field pattern is indistinguishable from that of normal circular top dots.<sup>14</sup> They have been occasionally found to fail by shorting out,<sup>15</sup> probably with greater frequency than the traditional design. The uncontrollable nature of the zinc oxide layer at the 'step' where the connecting strip crosses the edge of the counter-electrode below may explain this. See Fig. 1-6(e).

Images were taken at 3.0 - 3.6 GHz with two lenses incorporating this type of transducer. The lenses had 16  $\mu$  and 19  $\mu$  radius. In the case of the 16  $\mu$  lens, the working space, or distance from lens to scanning sample, was 13  $\mu$  at focus. As an example, acoustic images of a MOS on sapphire transistor are shown in Fig. 2-7. The acoustic frequency for the two pictures on the left is 3.5 GHz, with a corresponding wavelength of 4400 Å and an expected resolution 3500 Å. The acoustic lens radius was 19  $\mu$ . The optical picture on the right of Fig. 2-7 is an oil immersion photograph and exhibits better resolution than the acoustic pictures.

The difference in contrast between the acoustic pictures results from being taken at different focal positions. In the left photograph the lens is focused on the bright central gate region of the transistor, which is higher than the drain and source regions on either side. These are in focus in the center photograph. The central gate region in each photograph is 7  $\mu$  across, or 20 times the expected resolution of the

acoustic micrographs. Examination of the fine structure in the left acoustic picture shows detail consistent with the expected resolution.

The central picture in Fig. 1-7 exhibits interference effects. Note the change from light to dark in the sapphire substrate on either side of the gate. This interference is with the 'flat' pulse, to be examined next, rather than with the lens-water interface return, which was kept sufficiently narrow by the new offset bond pad transducer design. Finally, in the top of the optical picture at right, taken after the acoustic pictures, we note the result of a grazing contact between acoustic lens and sample. This hazard, always potentially present in a scanning system, is worse with very small lenses, but even here care and operator experience makes collisions infrequent.

A final difficulty to overcome with high frequency imaging is the presence of an interfering pulse from the flat region around the outside of the hemispherical lens. In Fig. 2-8 we show the hemispherical lens ground in sapphire surrounded by a small flat region which is left on the rod to protect the lens edge, which would be more easily damaged without it.

The incoming plane wave in the sapphire is typically designed to be 3 dB down at the edges of the lens, and thus substantial power strikes the surrounding flat region. It is coupled into water through the glass matching layer which extends over the flat region. It is reflected back to the lens and gives rise to an output pulse at the transducer. This pulse precedes the focused pulse from the lens in time due to the shorter propagation path in water. It is also attenuated less than the focused pulse, again owing to the shorter path in water. It is often seen with

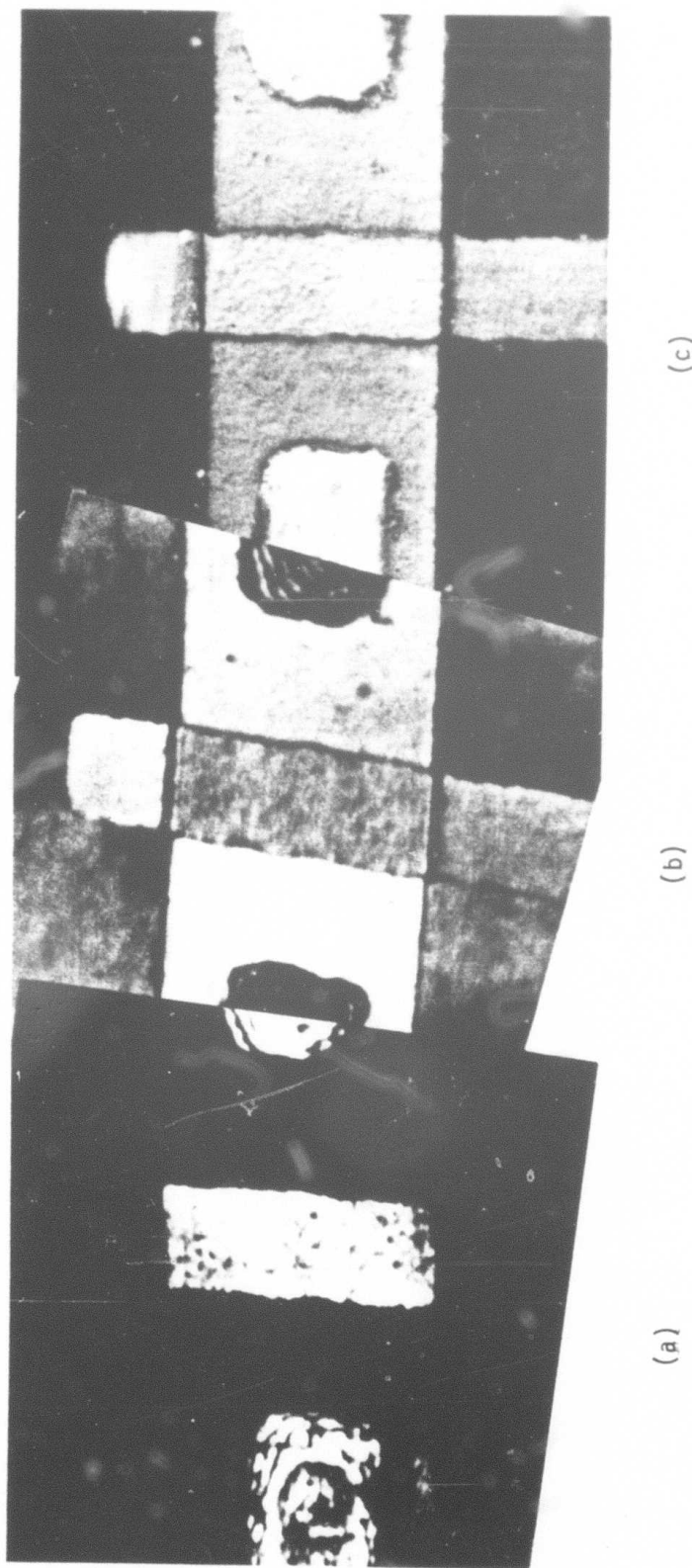


FIG. 2-7. Gate region of FET transistor; (a) and (b) acoustic micrographs, 3.5 GHz, (c) optical oil immersion picture.

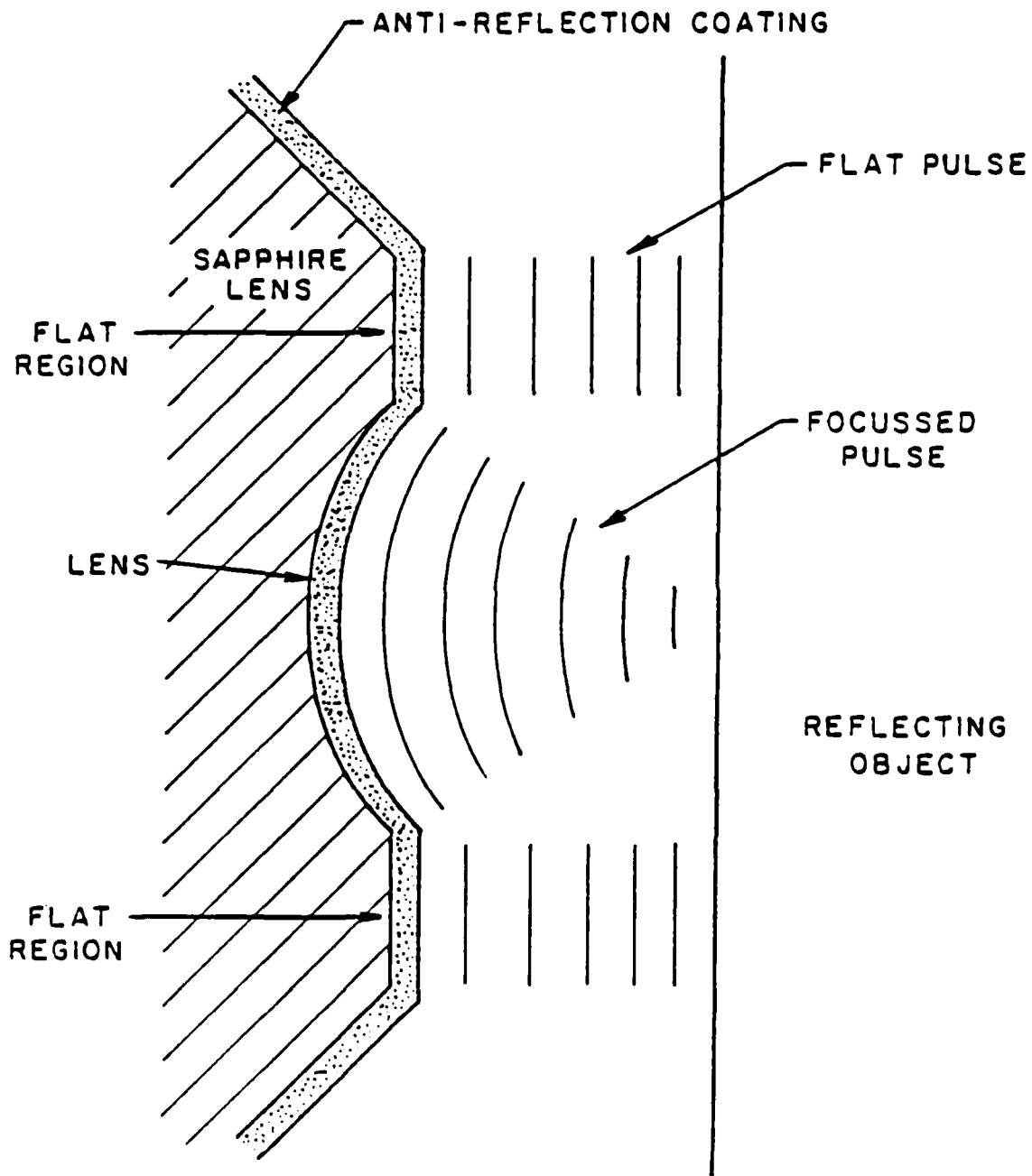


FIG. 2-8. Origin of the 'flat' pulse.

very small lenses. Its strength varies unpredictably from lens to lens, perhaps because of differences in the surrounding flat area and in lens illumination. It is recognized by its position in time and its failure to exhibit a focal position or a typical  $V(z)$  behavior.

The 'flat' pulse precedes the focused pulse by approximately:

$$\Delta t = \frac{2r(1 - \cos \theta)}{V_s}$$

where  $r$  = lens radius,  $\theta$  = lens opening angle, and  $V_s$  = speed of sound in water. For a  $20 \mu$  lens with opening angle  $50^\circ$ , this time delay is 10 nsec, and smaller proportionally as the radius. The 'flat' pulse is typically 20 dB below the focused pulse, but if one moves off focus the two pulses may be comparable in size. The interference of the falling edge of the 'flat' pulse with the focused pulse in this situation is severe.

Two possible remedies to eliminate the 'flat' pulse can be mentioned. The most straightforward approach is to coat the flat region around the outside of the lens with an acoustic absorber. A disadvantage of this is the likelihood that contact with the scanned sample would scrape this layer off. Special application with a micro-manipulator would likely be necessary because of the tiny dimensions concerned. A second remedy would be to coat the entire sapphire blank surface with a  $\lambda/4$  layer of glass before lens grinding. This layer would of course be removed in the lens itself. After the sputtered glass anti-reflective coating was applied, the flat area would be covered with a high reflectivity



$\lambda/2$  layer of glass. A disadvantage here is that the lens-water interface reflection pulse b in Fig. 2-5 would be increased, thereby worsening any interference with that pulse.

To summarize work on high frequency acoustic microscope operation, acoustic images have been taken in water with lenses of radius as small as  $16\ \mu$ , at frequencies as high as 3.6 GHz, where  $\lambda = 4300\ \text{\AA}$  and the resolution is  $3500\ \text{\AA}$ . The new design of transducers which removes bonding from the top electrode to an adjacent bond pad has reduced the broadening of the pulse by acoustic echos from the bond itself. This broadening is no longer the major degrading influence on the imaging performance of present lenses smaller than  $30\ \mu$  radius. The problem of a 'flat' interference pulse has replaced the transducer-induced broadening as the most important source of image degradation in acoustic microscopy at high frequencies.

## REFERENCES FOR SECTION 2

1. R.A. Lemons and C.F. Quate, "Acoustic Microscopy," in R.N. Thurston, ed., Physical Acoustics, vol. 14, New York: Academic Press, 1979.
2. A. Atalar, Acoustic Reflection Microscope, Ph.D. Thesis, Stanford University, 1978.
3. V.B. Jipson and C.F. Quate, "Acoustic Microscopy at Optical Wavelengths," Appl. Phys. Lett. 32, 789 (1978).
4. W.J. Smith, "Image Formation: Geometrical and Physical Optics," in W.G. Driscoll and W. Vaughn, eds., Handbook of Optics, New York: McGraw-Hill, 1978, pp. 2-35.
5. Reference 4, pp. 2-28.
6. J. Attal and C. F. Quate, "Investigation of Some Low Ultrasonic Absorption Liquids," J. Acoust. Soc. Am., 59, 69 (1976).
7. V.B. Jipson, "Acoustic Microscopy of Interior Planes," Appl. Phys. Lett. 35, 385 (1979).
8. J. Attal, private communication.
9. J. Heiserman, D. Rugar, and C.F. Quate, "Cryogenic Acoustic Microscopy," J. Acoust. Soc. Am. 67, 1629 (1980).
10. V.B. Jipson, private communication.
11. V.B. Jipson, Acoustic Microscopy at Optical Wavelengths, Ph.D. Thesis, Stanford University, 1979, pp. 26-38.
12. F.N.H. Robinson, Noise and Fluctuations in Electronic Devices and Circuits, Oxford: Clarendon Press, 1974, pp. 196-197.
13. Reference 10, pp. 55-60.
14. D. Rugar, private communication.
15. D. Rugar and L. Lam, private communications.

## SECTION 3

### MATERIALS STUDIES WITH ACOUSTIC MICROSCOPY

#### 3.1 Introduction

Acoustic microscopy reveals new information about small objects. The source of contrast in the acoustic reflection microscope is the  $V(z)$  response of a sample. The  $V(z)$  response contains the amplitude and phase of the sample reflectance function  $R(\theta)$  for all angles within the lens opening angle.

Reflectance for acoustic plane waves is, in turn, determined by mechanical properties of the sample. In particular the density and the stiffness tensor, or equivalently sound velocities and impedance determine the reflectance of a sample for plane waves of sound incident in a liquid. In addition the mechanical integrity of a bond at a layer interface will strongly influence the sound reflectance, as we shall study in detail in Section 4. If our sample is lossy this information is also in the reflected signal. In all, we can characterize our pictures as maps of the variation in mechanical properties of a sample on a microscopic scale. They are topographical maps as well because of the reflection microscope's sensitivity to  $z$  position.

Optical micrographs are maps of a different set of material properties. It is well known that a transparent object immersed in a liquid with identically the same index of refraction is invisible. Contrast in the optical microscope comes from variations in the index of refraction or in the optical absorption or scattering properties of a sample.

These are all dielectric properties telling us how the sample interacts with electromagnetic radiation.

The transmission electron microscope (TEM) presents us with high-resolution images of the electron absorption coefficient of a thin sample. The scanning electron microscope gives us a map of secondary electron production from a scanned incident electron beam.

All these microscopic imaging methods are complementary in that they are local maps of the variation in different properties of a sample. In this section and the next we present acoustic microscopy of several types of samples: metallurgical samples, composite materials, layered structures, and films with doubtful adhesion. In each case we will see that acoustic microscopy reveals information that is either more difficult or impossible to obtain by other means.

### 3.2 Metallurgical Samples

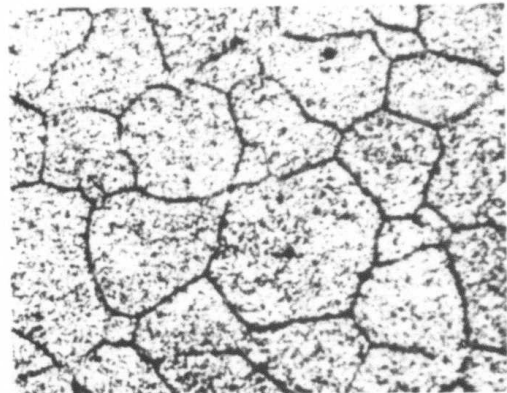
In Fig. 3-1 we show four micrographs of an inconel (Ni/Cr/Fe) alloy. The width of the field of view is 140  $\mu$  in each case. The areas are different but representative. Figure 3-1(a) is an optical micrograph of the polished surface. There is little structure visible except surface scratches from the polishing operation.

To make the microstructure visible to optical microscopy the surface may be etched chemically, as was done for Fig. 3-1(b). Here a 5% Nitral electrolytic etch was performed. The etchant leaves a fine precipitate within the grains and etches the grain boundaries more rapidly. Thus the grain boundaries are made visible for optical microscopy by the etching process. The etch rate is the same for the different grains, however, so there is no contrast from grain to grain.

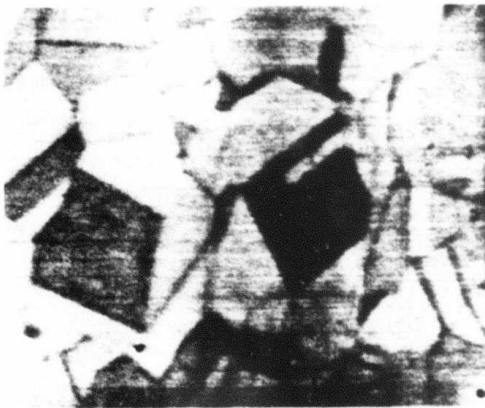
INCONEL ALLOY



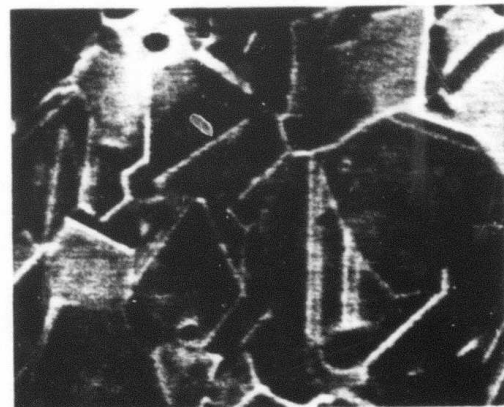
(a) OPTICAL , POLISHED



(b) OPTICAL , ETCHED



(c) ACOUSTIC  $Z = -0.5 \mu$   
2.7 GHz



(d) ACOUSTIC  $Z = -1.0 \mu$   
2.7 GHz

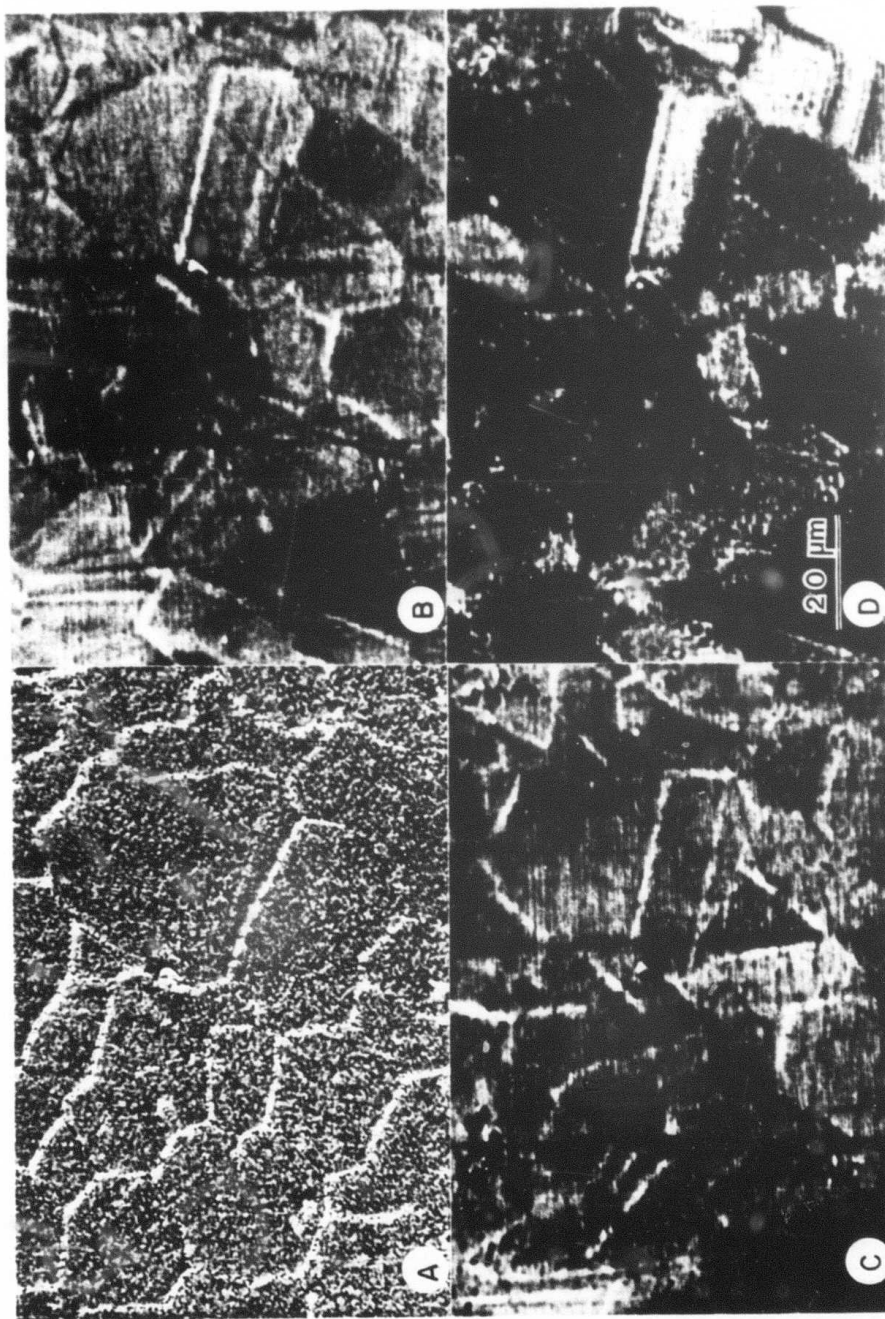
FIGURE 3-1

Acoustic reflection microscope images of the polished but unetched inconel sample are shown in Fig. 3-1(c) and Fig. 3-1(d). The images were taken with lens (c) of Table 2-1. We have a large degree of contrast between grains in both images. The grain boundaries are clearly visible. There is structure clearly visible within individual grains. In particular, note the two sets of bright parallel lines running vertically in the lower right of Fig. 3-1(d). These are twin planes where there is a mirror symmetry relationship between the crystal orientation on opposite sides of the twinning plane.<sup>1</sup> This is a different type of feature from a grain boundary. On opposite sides of a given boundary there is, in general, no relationship between the orientation of the crystalline axes.

Twin lines within grains may be made visible by electrolytic etching as well, if the etchant is chosen carefully.<sup>2</sup>

In Fig. 3-2 we show one optical picture (a) and three acoustic microscope reflection pictures of the same area of an inconel sample. The acoustic pictures were taken first, before the sample was electrolytically etched in 5% Nital solution. Then the optical picture of the etched sample was made. The etching process brings out the grain boundaries. Subtle indications of twin lines within grains are visible in some places.

The acoustic pictures (taken with lens D) have different contrast because they are taken at different  $z$  position, and we saw in Chapter 2 that contrast in acoustic reflection images is highly sensitive to where we are operating on the  $V(z)$  graph. The acoustic images reveal structure within grains that is simply not visible in the optical



Inconel alloy. (a) Optical micrograph after etching (b), (c), (d) 2.5 GHz acoustic micrographs of unetched sample at 3 different focal positions ( $z = -1 \mu$ ,  $-2 \mu$ ,  $-4 \mu$ ).

FIGURE 3-2

micrograph of the etched sample. The lower right corner of the acoustic images in particular reveal a wealth of structure within areas shown by the optical image to be single grains.

Another distinctive feature of the acoustic micrographs in Figs. 3-1 and 3-2 is the relatively large contrast from grain-to-grain. This contrast is completely lacking from the optical micrographs. The fact that all grains in the optical micrographs have been etched to the same depth indicates that this is a homogeneous alloy. The same chemical composition is characteristic of all the grains. We attribute the acoustic contrast between different grains that we see in Figs. 3-1 and 3-2 to difference in crystalline orientation. This means that the  $V(z)$  curve for imaging a flat crystal face depends on the orientation of the crystalline A, B, C axes relative to the normal to the face. For anisotropic crystals we know the stiffness tensor components are a strong function of crystal orientation. We expect a dependence of reflectance, and thereby the  $V(z)$  curve also, upon grain crystalline orientation. Atalar<sup>3</sup> in studies of single-crystal silicon, was able to show a difference between measured  $V(z)$  for (100) silicon and (111) silicon.

In Fig. 3-3 we see three images of the same area of a polycrystalline silicon sample. The horizontal band across the bottom of each image is an identification mark. The optical micrograph of the polished but unetched surface at the top shows little but surface scratches. The acoustic micrograph (taken with lens D in Table 2-1) at the center is of the polished, unetched sample. The vertical line in this picture is an artifact from the scanning electronics. The diagonal black line and the





(Top) Optical micrograph of polished Si sample.  
(Center) Acoustic micrograph of same area  $f = 2.5$  GHz .  
(Bottom) Optical micrograph of same area after etching.

FIGURE 3-3

curving white line are new features brought out by the acoustic microscope. These are revealed to be a grain boundary (the white curving line) and a twin line (the diagonal black line) by the optical micrograph of the etched sample below.

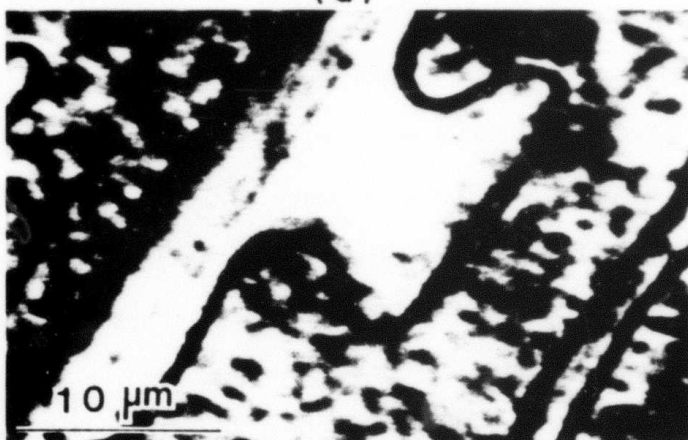
In this case the acoustic micrograph was not able to resolve as much of the microstructure of the sample, but it was able to resolve some of it nondestructively.

In Fig. 3-4 we present optical and acoustic micrographs of the same region of a germanium/aluminum two-phase alloy. In Fig. 3-4(a), the optical micrograph, the germanium-rich phase appears dark and the aluminum-rich phase is light. The dendritic pattern is characteristic of this alloy. In Fig. 3-4(b), a white region appears between parallel lines in the germanium phase. These parallel lines are brought out by the acoustic micrograph in Fig. 3-4(c). From etching studies of this alloy, twinning planes have been found in similar positions within the germanium phase of this alloy.<sup>2</sup> We conclude that these are, in fact, twinning planes not visible in the optical micrograph of the unetched sample in Fig. 3-4(a).

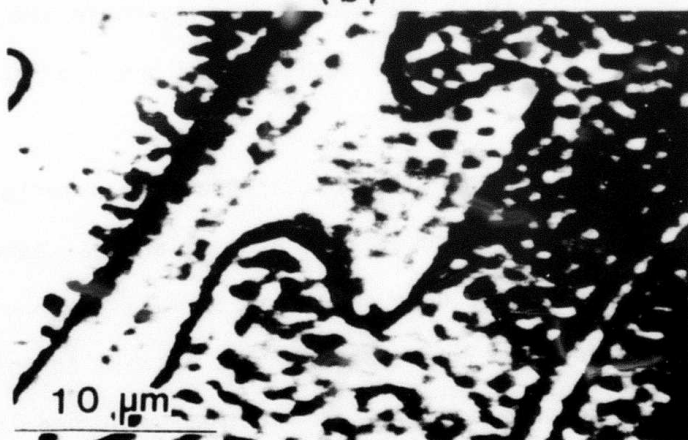
Grain boundaries, twinning planes, crystalline orientation and other features of the microstructure of a metallurgical sample are mechanical features which we have shown can be made visible by acoustic microscopy. These features are typically not visible to optical microscopy except after the samples have been chemically etched in a manner that destroys the surface polish.



(a)



(b)



(c)

FIG. 3-4. Micrographs of Ge/Al Alloy. (a) Optical, (b) and (c) Acoustic micrographs (2.6 GHz).

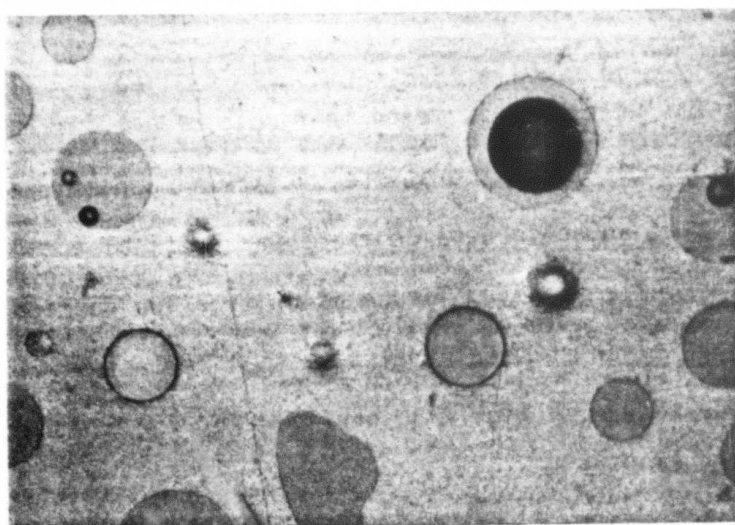
### 3.3 Composite Materials

Many solid samples have sound velocity and acoustic impedance much higher than water. This means that most of the incident energy in our focused beam is reflected at the surface. Much of the focused beam energy is at an angle outside the shear critical angle for the solid where the reflectance amplitude is unity. The portion of the beam within the shear critical angle is still reflected with high reflectance, as we see in Fig. 2-3, or Fig. 2-5, for example.

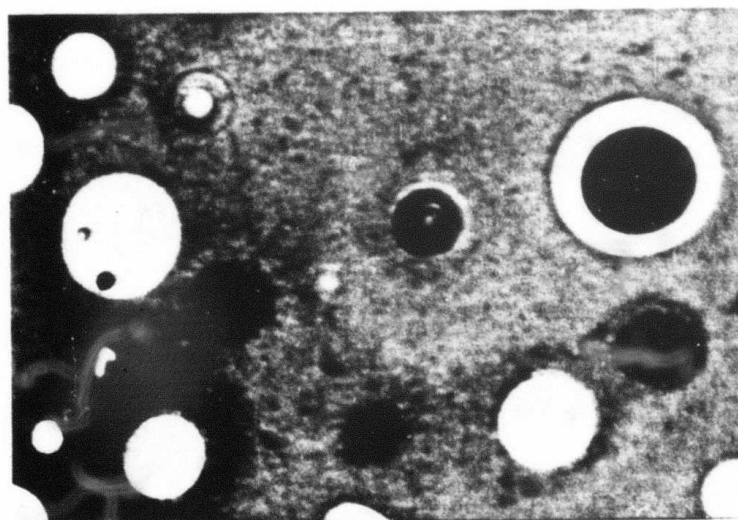
We have seen in Section 2 that even in the case of high-impedance solids such as silicon, the reflectance and therefore the  $V(z)$  are sensitive to a subsurface layer. This was because the subsurface layer was a small fraction of a wavelength below the surface.

If we attempt to image structures deep within a solid with our microscope, we are confronted with the previously mentioned high reflectance at the surface. We also have the problem of severe spherical aberration with the portion of the beam inside the shear critical angle. Jipson circumvented these difficulties by using liquid gallium in the microscope. He was able to image through a  $75\mu$  thick piece of fused quartz with both the longitudinal and shear waves in the quartz.<sup>4</sup>

In the case of low-velocity materials the acoustic microscope with water can be used to image interior structures. In Fig. 3-5 we see optical and acoustic micrographs (taken with lens D in Table 2-1) of a composite material consisting of hollow glass spherical beads imbedded in polyethylene. The sample has been cleaved to achieve a flat front surface that slices through many of the beads. The acoustic picture shows several subsurface beads not seen in the optical picture.



(a) OPTICAL x620



(b) ACOUSTIC (2600 MHz)

POLYETHYLENE TEREPHTHALATE  
WITH IMBEDDED GLASS BEADS

FIGURE 3-5

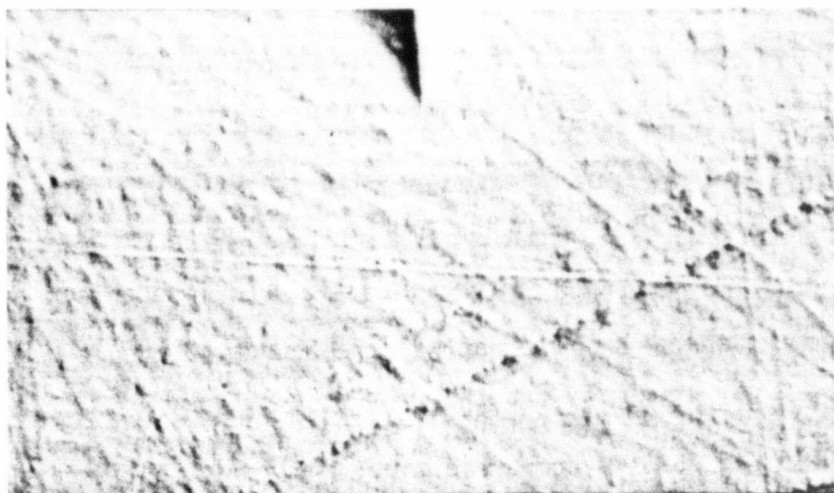
Polyethylene has a longitudinal sound velocity of 1900 m/sec and acoustic impedance  $1.9 \times 10^6$  mks rayl,<sup>5</sup> compared with water velocity 1540 m/sec and water impedance  $1.54 \times 10^6$  mks rayl. The good velocity match means negligible aberration is introduced by the refraction at the polyethylene/water interface. The good impedance match means efficient energy transfer across the boundary. Hence we are able to image beads below the surface.

In Fig. 3-6 we compare optical and acoustic micrographs of another composite material consisting of much smaller ( $\sim .25\mu$  diameter) glass beads in a polyethylene matrix.<sup>6</sup> In the optical micrograph in Fig. 3-6(a) we have almost no structure visible except surface scratches. An occasional small bead shows on the surface. In Fig. 3-6(b) the acoustic image reveals that the polyethylene contains a very high density of these beads. The beads are beyond the resolution limit of the acoustic microscope at 2.6 GHz in water, in the sense that two beads in contact would not be resolved as separate. They still act as scattering centers, however, so in Fig. 3-6 their presence is evident.

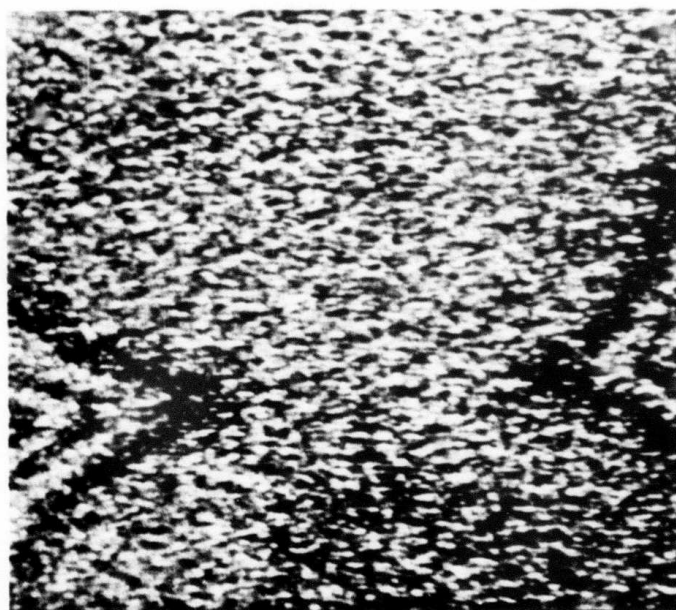
### 3.4 Layered Structures

Many important microscopic structures consist of a pattern of plane layers on a substrate. All integrated circuit structures fall into this category, for example. We have seen that the acoustic microscope image of a layered structure contains information about subsurface conditions.

In Fig. 3-7 we see an aluminum line  $1\mu$  thick on a silicon substrate with a  $2\mu$  sputtered glass overlay.<sup>7</sup> The acoustic images were



(a) OPTICAL



(b) ACOUSTIC

FIG. 3-6. Micrographs of a composite material consisting of  $\sim 0.25\mu$  glass beads imbedded in polyethylene. Field of view is  $70\mu$  wide. (a) and (b) are different areas.

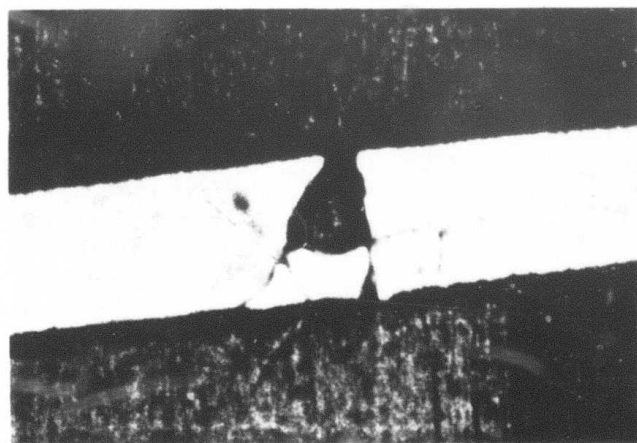
taken with lens D of Table 2.1. The line is  $15\mu$  wide. It has been intentionally damaged with a diamond indenter as part of an electromigration study. The optical micrograph in Fig. 3-7(b) is an oil immersion interference contrast picture. Of special interest in the acoustic image in Fig. 3-7(a) is the network of cracks in the aluminum line which are not evident in the optical image of Fig. 3-7(b). The dark area of the indentation in Fig. 3-7(a) is seen to be different in its acoustic response from the other indented areas and from the rest of the aluminum line. A possible explanation is that the indenter has broken loose the bond between the aluminum and the silicon below or between the aluminum and the quartz above. As we shall see in a more controlled study in Section 4, adhesion failure gives rise to strong contrast in acoustic micrographs. An alternate possibility is that the indenter has removed the glass layer from this area.

In the acoustic image of Fig. 3-7(c) we see a series of cracks in the silicon substrate radiating away from the indentation. There is no indication of these cracks in the optical picture.

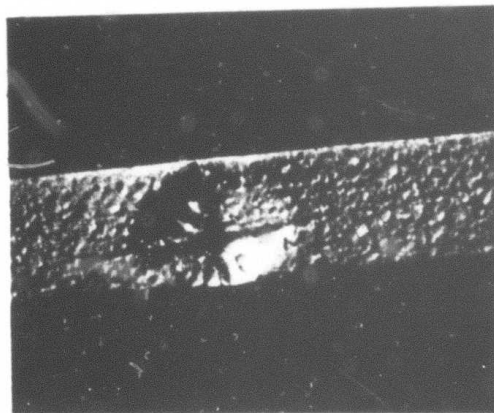
In Fig. 3-8 we see an aluminum sample which has been anodized with a  $\sim 5\mu$  layer of  $Al_2O_3$ . The sample has been struck twice with a diamond indenter. The aluminum has undergone plastic flow in the process. This has been shown<sup>2</sup> to leave a residual stress in the oxide layer which may crack, but does not undergo plastic flow.

The ring-shaped patterns in the two acoustic pictures (Fig. 3-8(b) and Fig. 3-8(c)) are hauntingly reminiscent of stress patterns observed in photoelastic studies.<sup>8</sup> They are not, however, unambiguous proof that we have observed stress with the acoustic imaging process. The ring-shaped patterns could equally well be a result of the unlevel

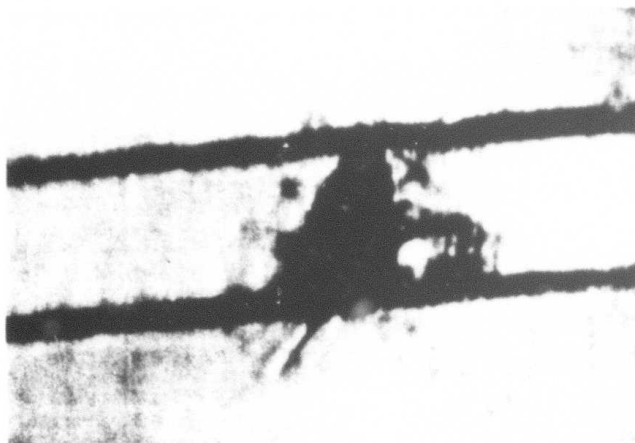




(a) ACOUSTIC  
1<sup>st</sup> FOCUS



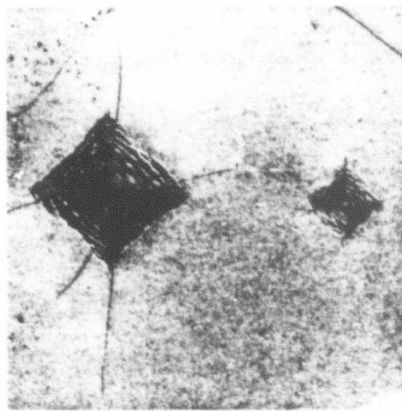
(b) OPTICAL



(c) ACOUSTIC  
2<sup>nd</sup> FOCUS

# ALUMINUM LINE ON SILICON WITH QUARTZ OVERLAY

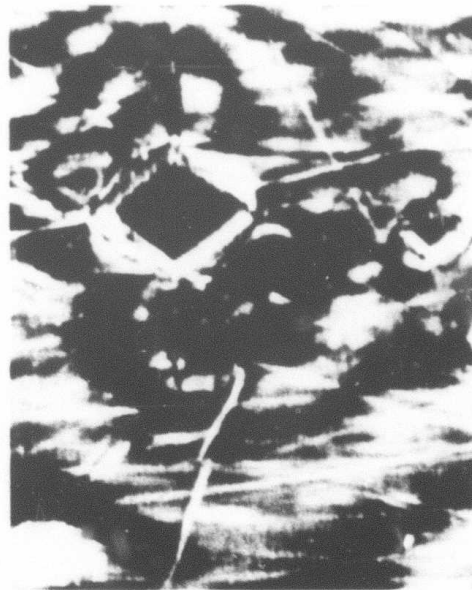
FIGURE 3-7



(a) OPTICAL (POLARIZED LIGHT)  
FIELD IS  $325 \times 325 \mu\text{m}$



(b) ACOUSTIC FOCUS #1



(c) ACOUSTIC FOCUS #2

COMPARISON IMAGES FOR AN  
ALUMINUM SAMPLE WITH AN OXIDE LAYER

FIGURE 3-8

contour of the surface that was induced by indentation.

We note that there are unambiguous features in the acoustic micrographs not seen in the optical picture. In Fig. 3-8(c) we see a number of white straight lines running across the field. These are most likely scratches from the polishing operation on the aluminum surface below the oxide layer. They are invisible in the optical polarized light photograph of Fig. 3-8(a), which was taken after the acoustic micrographs.

### REFERENCES FOR SECTION 3

1. W.G. Moffatt, et al., The Structure and Properties of Materials, Vol. 1: Structure, New York: Wiley, 1964, pp. 92-93.
2. Rosemarie Koch, private communication.
3. A. Atalar, Reflection Acoustic Microscope, Ph.D. Thesis, Stanford University, 1978, p. 106.
4. V. Jipson, "Acoustic Microscopy of Interior Planes," Appl. Phys. Lett. 35, 385 (1979).
5. KB-Aerotech Transducer Technology Center, "Velocity and Acoustic Impedance Table," Lewistown, PA: n.d.
6. G.J. Sloan, Dupont Co., Wilmington, DE, private communication.
7. Jim Lloyd, IBM Co., E. Fishkill, N.Y., private communication.
8. H.T. Jessop and F.C. Harris, Photoelasticity: Principles and Methods, New York: Dover, 1960, pp. 142,156.

## SECTION 4

### ADHESION STUDIES WITH THE ACOUSTIC MICROSCOPE

#### 4.1 Introduction

Adhesion is attachment or the act of sticking. The proper functioning of many devices depends on the adhesion of a layer or film to a substrate. In the present section we devote brief attention to some of the traditional methods for measurement of adhesion. Then we present results of adhesion studies with acoustic microscopy. We find that degree of adhesion of Cr films on glass represents a direct source of contrast in acoustic micrographs. We believe acoustic microscopy offers a new and useful nondestructive method for evaluation of thin film adhesion. This work as mentioned briefly in the last quarterly, has attracted widespread interest and we therefore want to expand our discussion.

#### 4.2 Adhesion Measurement

A handbook table lists the following techniques that have been used for measurement of adhesion: bending, squashing, abrasion, heating and quenching, scratching, hammering, indentation, pulling, peeling, deceleration, blistering.<sup>1</sup> With all these techniques, sufficient stress is applied to remove the film from the substrate and a conclusion regarding degree of adhesion is reached. We note the inherently destructive character of the measurement.

In the category of 'peeling' is the most common adhesion test, the 'scotch tape' method.<sup>1,2</sup> In this test a piece of tape is pressed on the film and then pulled off. The film is either wholly removed

partly removed, or not removed. This is a crude 'go - no go' approach, but it is easy and fast.

In scratch methods,<sup>1,4</sup> a variable load on a stylus is applied to a film on a substrate. The stylus is drawn across the substrate in a series of scratches with increasing loading. Subsequent examination with optical microscopy reveals the load necessary to completely remove a channel of the film. This load is termed the critical load and is then a measurement of degree of adhesion.

In deceleration methods,<sup>1,2</sup> the film and substrate are subjected to increasingly violent deceleration by ultracentrifuge or ultrasonic vibration. The deceleration force necessary to remove the film characterizes degree of adhesion.

In the laser spallation<sup>5</sup> method of film adhesion measurement, an optical absorber is deposited on the back side of a substrate. On the front side of the same substrate is a film whose adhesion is to be measured. A very high energy laser pulse is used to explosively evaporate a portion of the absorbing material on the back of the substrate. This generates a high energy shock wave which propagates to the front surface. The reflection of this shock wave causes the substrate to snap back in tension. The laser pulse energy is increased until the adhering film is blasted off.

All these methods provide quantitative or qualitative tests of adhesion. The acoustic microscope will be seen to offer nondestructive evaluation of film adhesion.

#### 4.3 Acoustic Microscopy of Film Adhesion

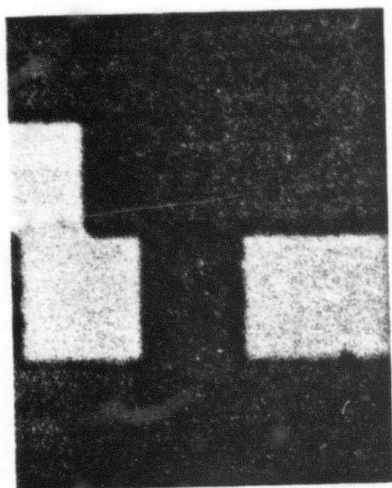
In the present study<sup>9</sup> production masks for photolithography in integrated circuit fabrication were examined with high resolution acoustic and optical microscopy.

The masks consisted of patterns of 1000 Å thick chromium films evaporated on low expansion glass substrates. Certain of the samples were known to consist of well adhered chromium, while others were known to have poorly adhering chromium. Adhesion was first noted by inspection for missing parts of the known mask geometry. It was then measured with the tape test<sup>1,2</sup> and scratch test<sup>4</sup> to qualitatively determine degree of adhesion.<sup>6</sup>

For acoustic imaging we have used the reflection mode microscope with an acoustic frequency of 2.5 GHz and a corresponding acoustic wavelength in 60°C water of 6000 Å. The acoustic lens radius was 22 microns, with an opening angle of 50 degrees, making an  $f/0.75$  lens. The resolution observed with this lens under these conditions is about 5000 Å. This is lens B of Table 2.1.

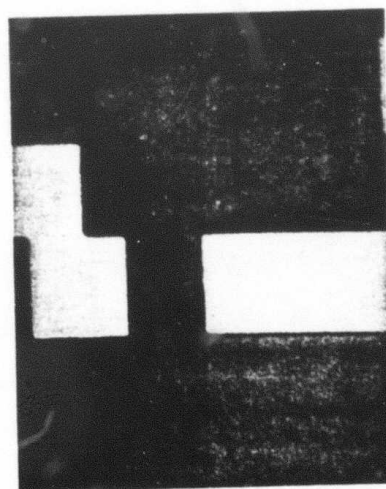
Images of well adhered 1000 Å thick chromium patterns on glass are shown in Fig. 4-1. In both the optical and the acoustic images of the same region of a Cr/glass mask, uniformity of brightness over the area of each material is evident. This indicates a uniformity of acoustic reflectance over the Cr-covered areas, and hence a uniformity of mechanical properties, including film adhesion. The reversal of contrast in the acoustic images for different spacings between the object and the focal plane is easily understood in terms of the  $V(z)$  response

1000 Å Cr ON GLASS (GOOD ADHESION)

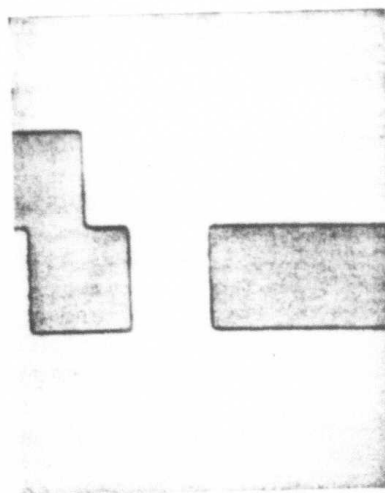


30 μm

(a) OPTICAL



(b) ACOUSTIC, FOCUSED ON Cr



(c) ACOUSTIC, FOCUSED ON GLASS

FIGURE 4-1



for glass and Cr/glass. This will be discussed in detail presently.

Comparative images of poorly adhering Cr on glass are shown in Figs. 4-2 and 4-3. In each of the optical images the contrast is quite uniform across the chromium-coated areas. There is surface dirt visible in the optical image of Fig. 4-2, but the primary indication of poor adhesion is the fact that areas of the pattern have actually peeled off and are missing.

In the acoustic images of Fig. 4-2 the glass has uniform brightness but the Cr patterns have strongly contrasting areas around the edges, which we believe are regions of poor adhesion. Nonuniformity of adhesion should result in nonuniform acoustic reflectance, resulting, in turn, in nonuniform brightness in the acoustic image.

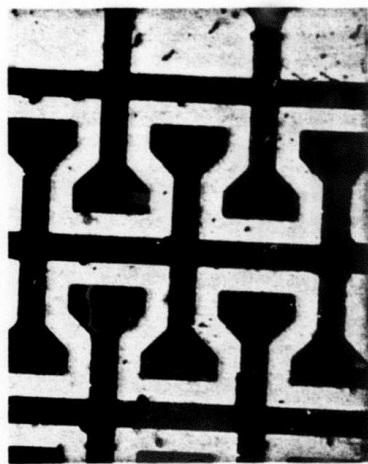
In Fig. 4-3 the optical micrograph shows excellent resolution of the surface texture of the chromium pattern at high magnification, but there is no indication of poor adhesion, either from contrast in the picture or missing areas of the chromium.

The acoustic micrographs of the identical region of the same sample do show regions of poor adhesion. In fact the masks in both Figs. 4-2 and 4-3 were determined to have poor adhesion as verified by the tape test.

#### 4.4 Interpretation of the Images

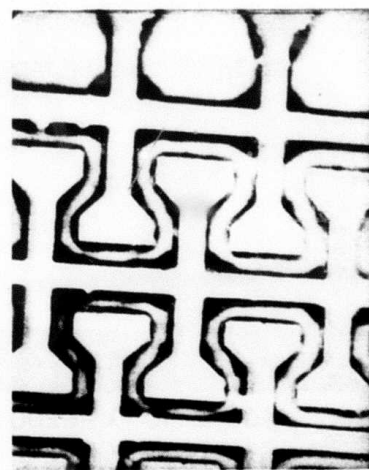
In Section 2 we graphed the reflectance function amplitude and phase (Figs. 2-3 and 2-4) and  $V(z)$  response (Fig. 2-9) for glass and 1000 Å Cr on glass. In Figs. 4-4(a) and 4-4(b) we see two acoustic micrographs of a 15  $\mu$  wide pad of Cr 1000 Å thick on glass. In the

1000 Å Cr ON GLASS (POOR ADHESION)

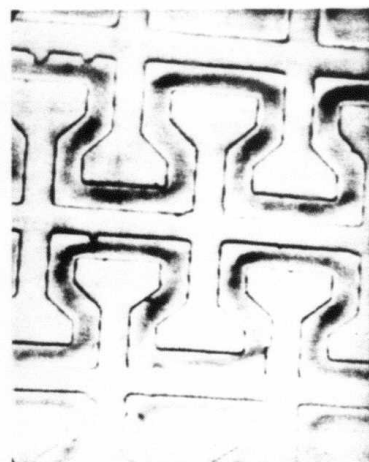


100  $\mu$

(d) OPTICAL



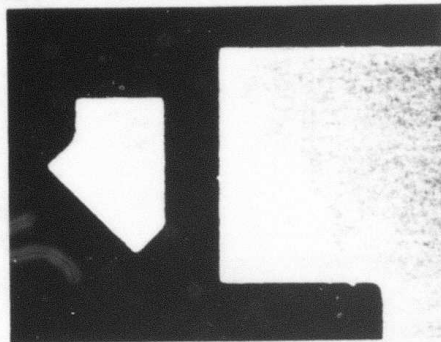
(e) ACOUSTIC  $Z = -1 \mu$



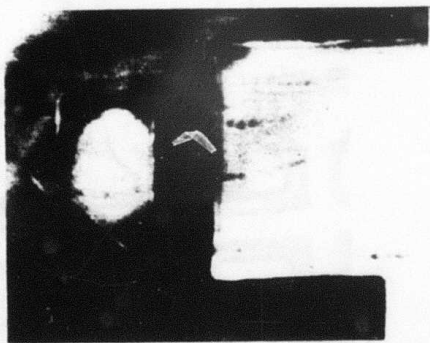
(f) ACOUSTIC  $Z = -0.5 \mu$

FIGURE 4-2

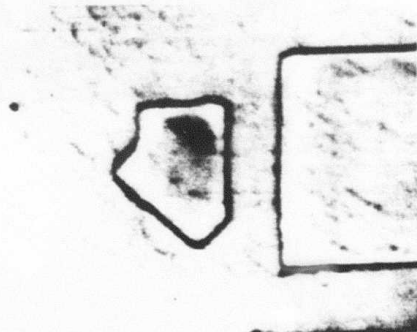
POORLY ADHERING CHROMIUM ON GLASS



OPTICAL OIL IMMERSION  
NA = 1.25 2600 X

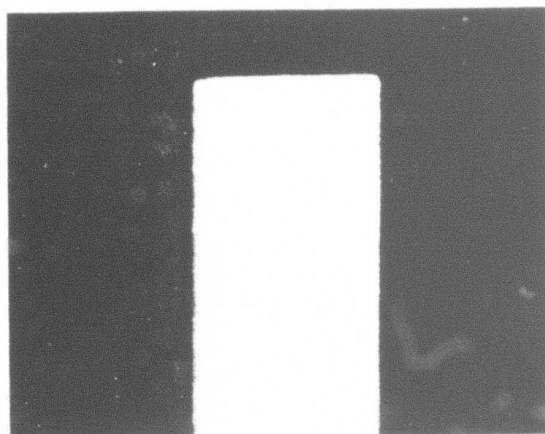


ACOUSTIC  $\lambda = 6200 \text{ \AA}$   
Z =  $-1 \mu$  2600 X

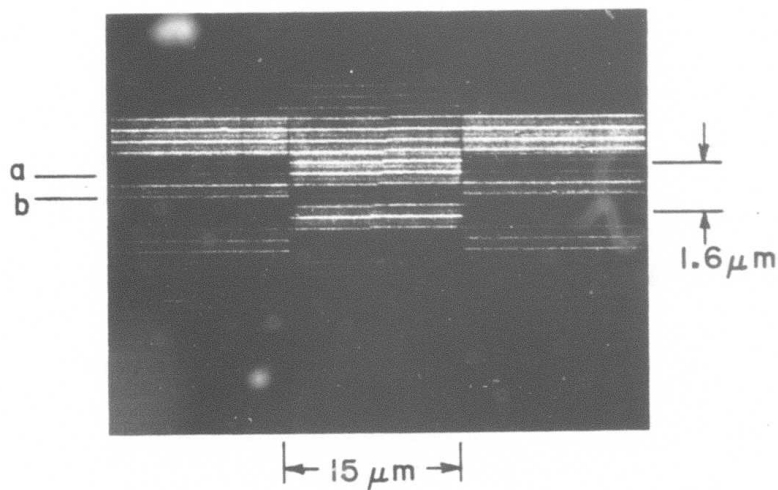


ACOUSTIC  $\lambda = 6200 \text{ \AA}$   
Z =  $+0.5 \mu$  2400 X

FIGURE 4-3



(a)



(b)

CHROME ON GLASS (1000 Å Cr)

FIGURE 4-4

center of Fig. 4-4 we have an experimental  $V(z)$  plot. To obtain this picture, the lens scanned along a single scan line across the Cr pad shown in Figs. 4-4(a) and 4-4(b). The lens was driven in the  $z$  direction toward the sample by a piezoelectric pusher. The same  $z$  drive signal controlled the vertical position of the CRT spot. The horizontal CRT spot location was controlled by the detected  $x$  position along the scan. The  $x$  scale is the same in all three pictures. Lens transducer output  $V$  controls intensity in the picture.

The  $V(z)$  graph for a single point on the scan line is then the intensity measured along a vertical line in the center picture in Fig. 4-4. The characteristic periodicity in intensity as we change  $z$  inside the focus is to be noted. This period for glass alone is different from the period for the Cr on glass region in the center. The micrograph in Fig. 4-4(a) was taken at the  $z$  position marked 'a' in the  $V(z)$  plot, while the micrograph of Fig. 4-4(b) was taken at the position marked 'b'. The features of this experimental  $V(z)$  plot are in good agreement with calculated graphs.

To model poorly adhering chromium, let us insert a thin layer of vacuum (or air) between the Cr and the glass substrate. Although the sample is in water at the time of imaging, the surface tension of water should prevent water penetration below a small area of Cr film. Stresses in the film may actually bow it out off the surface, however.<sup>7</sup> Stresses in evaporated thin films have been measured to be  $\sim 10^8 - 10^9$  dyn  $\text{cm}^{-2}$ ,<sup>3</sup> or 100 - 1000 atm. Hence a film whose adhesion to its substrate has failed is likely not in actual contact with the substrate.

In Fig. 4-5 we have graphed calculated  $V(z)$  for glass,  $1000 \text{ \AA}$  of Cr on glass, and Cr/vacuum/glass. The results shown in Fig. 4-5 correctly predict the contrast for regions shown in Figs. 4-1, 4-2, and 4-3. Note, for example, that at  $z = -1.5$ , the predicted Cr/vacuum/glass  $V(z)$  is 10 dB below the glass  $V(z)$ , and thus agrees with the darker poorly adhered region that we see in Fig. 4-3(b). On the other hand, note that in Fig. 4-3(c), the poorly adhered edges are brighter than the glass, which is in turn brighter than the central, better adhering part of the pattern. This relative contrast is in good agreement with that predicted by the model at  $z = -0.5$ .

#### 4.5 Conclusion

The reflectance of acoustic waves from layered structures depend strongly on the mechanical properties of those structures. This allows us to distinguish in the acoustic microscope those regions with different adhesion. We have developed a model for the reflection acoustic microscope which predicts that differing degrees of adhesion will have different reflection coefficients. Our simple model for a poorly adhered thin film predicts image contrast that is in good agreement with our observations.

The acoustic images demonstrate the power of the acoustic microscope as a new method for collecting information on the mechanical properties of microscopic structures. These are not readily available by other nondestructive techniques. Adhesion in particular is shown to be a strong source of image contrast.

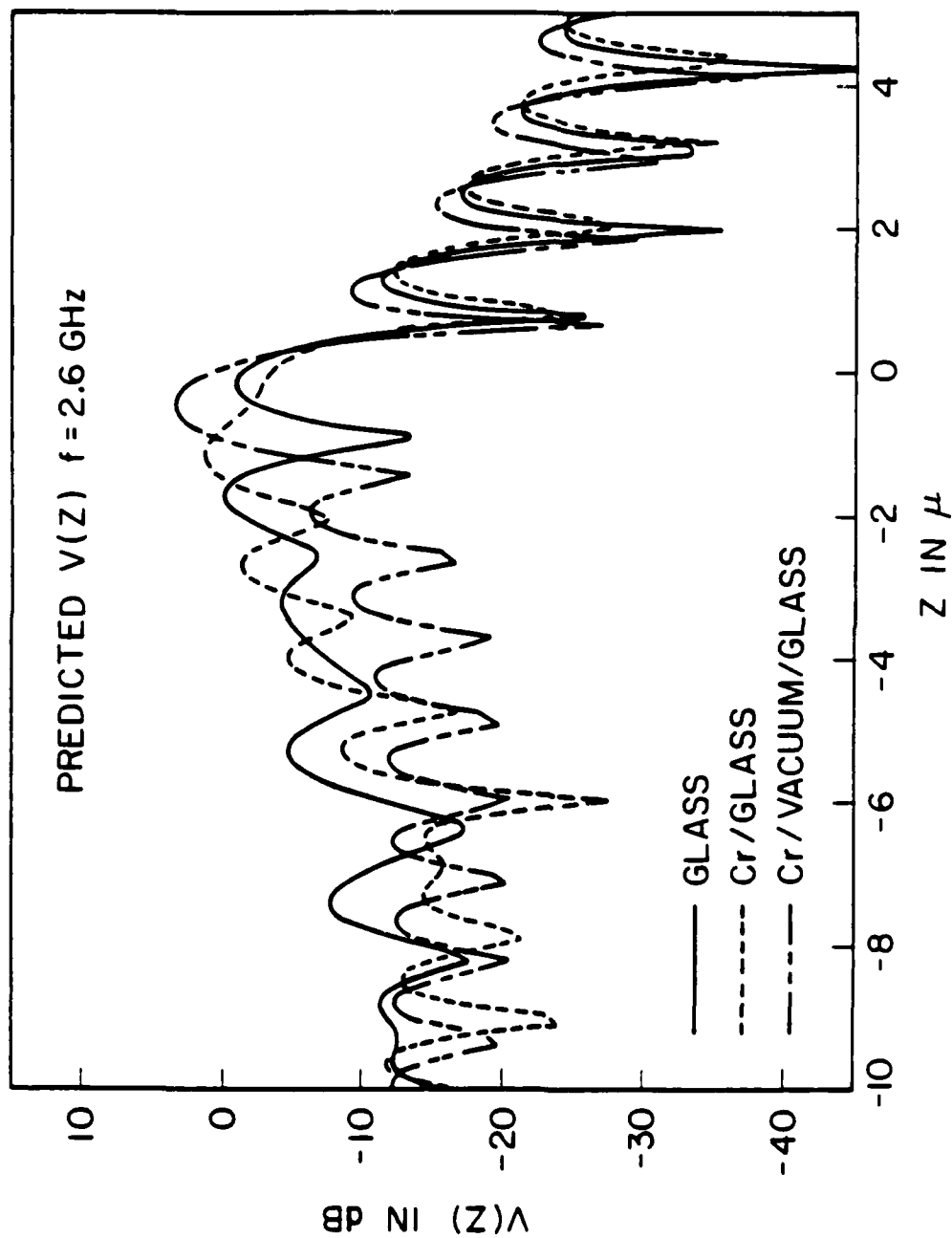


FIGURE 4-5

Our experience with acoustic reflectance and  $V(z)$  from a variety of layered structures indicates that film adhesion will be a source of acoustic image contrast whenever the layer thickness is smaller than the acoustic wavelengths in the layer, for any combination of layer and substrate. The technique should thus be widely applicable in microscopic evaluation of film adhesion.

Here we have used samples whose thin film adhesion was qualitatively known beforehand, from simple adhesion tests. Future studies should employ films whose mechanical properties are understood quantitatively through more controlled adhesion measurements.



#### REFERENCES FOR SECTION 4

1. D.S. Campbell, "Mechanical Properties of Thin Films," in Maissel and Glang, eds., Handbook of Thin Film Technology, New York: McGraw-Hill, 1970.
2. K.L. Mittal, "Adhesion Measurement of Thin Films," Electro-component Sci. Technol., 3, 21-42 (1976).
3. K.L. Mittal, ed., Adhesion Measurement of Thin Films, Thick Films, and Bulk Coatings, Philadelphia: ASTM, 1978.
4. J. Ahn, K.L. Mittal, and R.H. McQueen, "Hardness and Adhesion of Filmed Structures as Determined by the Scratch Technique," in Reference 3, p. 134.
5. J.L. Vossen, "Measurement of Film-Substrate Bond Strength by Laser Spallation," in Reference 3, p. 122.
6. J. Calhoun, Intel Corporation, private communication.
7. Reference 1, pp. 12-21 et seq.
8. Reference 1, pp. 12-36 et seq.
9. R.C. Bray, C.F. Quate, J. Calhoun, and R. Koch, "Film Adhesion Studies with the Acoustic Microscope," Thin Solid Films, 74, 295 (1980).

## SECTION 5

### THERMAL GENERATION OF SOUND

In our annual report, G.L. No. 3295 (July 1981), we introduced some of the relations which govern the flow of heat that is generated in the photoacoustic process. Here we will summarize some of the results concerning the generation of sound waves via the periodic variation of temperature. And in the following section we will present the experimental results that have been produced in the interval since the annual report was written.

The thermal waves described in the previous report (G.L. No. 3295) will generate propagating acoustic waves and we will work out the relations which determine all of this. The coupling is through the coefficient of thermal expansion. We denote it by the symbol,  $\beta$ . Hookes law governing the relation between the stress and strain can be written

$$T = c_{11}(S - \beta\theta) \quad (5.1)$$

where  $T \equiv$  stress,  $S \equiv$  strain accompanying the stress,  $\beta\theta$  is the strain component produced by the thermal expansion. The  $c_{11}$  is the elastic constant for longitudinal waves as given by  $c_{11} = \rho V_s^2$  where  $\rho$  is the mass density and  $V_s$  is the sound velocity.

The thermal waves have wavelengths that are widely different from the sound wavelengths and it is not obvious how the coupling between the two systems behaves but we can use the techniques described by Auld<sup>1</sup> when he worked out the coupling between the sound waves and electric fields for a piezoelectric medium. There the wavelengths of the two coupled systems are also widely different and the problem of coupling has similar features.

The analytical technique is based on normal modes which come from the differential equations that underlie sound propagation. We restrict ourselves to longitudinal waves propagating along to the z-axis as  $\exp(j\omega t - kz)$ . The differential equations relating the stress,  $T$ , to the particle velocity,  $U$ , are

$$\frac{\partial T}{\partial z} = -\rho \frac{\partial U}{\partial t} \quad (5.2a)$$

$$\frac{\partial U}{\partial z} = -\frac{\partial S}{\partial t} \quad (5.2b)$$

With Eq. (5.1) we replace  $S$  and write

$$\frac{\partial U}{\partial z} = -\frac{1}{c_{11}} \frac{\partial T}{\partial t} - \beta \frac{\partial \theta}{\partial t} \quad (5.3)$$

Since the sound waves and the thermal waves both vary with time as  $e^{j\omega t}$ , we can replace  $\partial/\partial t$  by  $j\omega$  and write

$$\partial T / \partial z = -j\omega \rho U \quad (5.4a)$$

and

$$\partial U / \partial z = -j \frac{\omega}{c_{11}} T - j\omega \beta \theta \quad (5.4b)$$

For the normal mode we multiply Eq. (5.4a) by the parameter  $Z_0$  and add to Eq. (5.4b)

$$\frac{\partial}{\partial z} (T + Z_0 U) = -j \frac{\omega Z_0}{\rho V_s^2} T - j\omega \rho U - j\omega \beta Z_0 \theta \quad (5.5)$$

The parameter  $Z_0$  is the acoustic impedance of the medium. It is equal to  $\rho V_s$ . With this we write

$$\frac{\partial}{\partial z} (T + Z_0 U) = -j \frac{\omega}{V_s} (T + Z_0 U) - j \frac{\omega}{V_s} c_{11} \beta \theta \quad (5.6)$$

The boundary conditions at the interface require the continuity of both stress,  $T$ , and particle velocity,  $U$ . These relations are sufficient to calculate the intensity of the waves that result from this form of generation. The boundary conditions at the interface require the continuity of both stress,  $T$ , and particle velocity,  $U$ . These relations are sufficient to calculate the intensity of the waves that result from this form of generation.

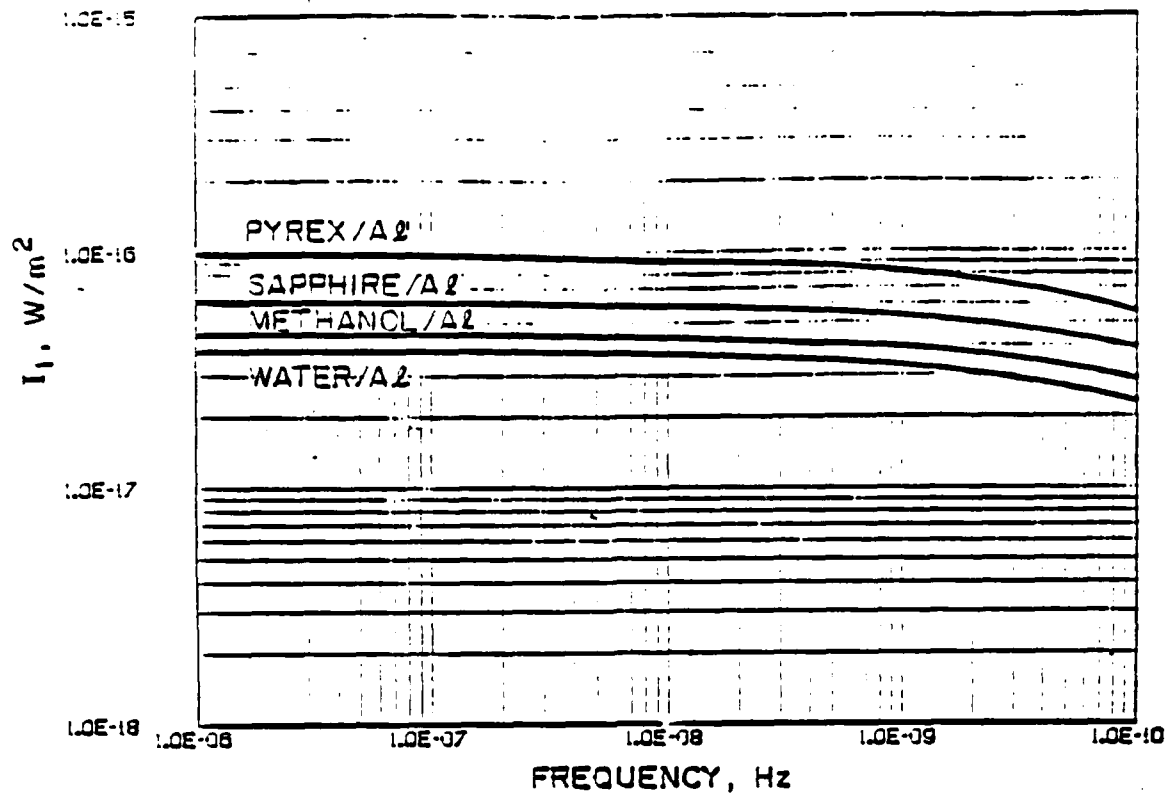
The outcome of all these calculations are best summarized in the set of curves in Fig. 5-1 and Fig. 5-2. There we consider a single interface between two media. The light with an intensity of 1 watt/mtr<sup>2</sup> is absorbed at the interface in medium 2 with an absorption length of  $1/\alpha$  meters. We can see there, Fig. 5-1a), that the sound intensity in medium 1 (approaching  $10^{-16}$  watts/mtr<sup>2</sup>) is nearly independent of frequency over the frequency range as shown. This means that we can choose the modulating frequency on the basis of some other criteria. For our case, it is the resolving power that we want to optimize.

We keep in mind that the light is absorbed in media 1. In Fig. 5-1(b) we find the plot of the sound intensity in media 2. The decrease over that in Fig. 5-1(a) is mostly accounted for by the acoustic impedance match at the boundary.

In Fig. 5-2 we find the data plotted for various other values of the important parameters. In Fig. 5-2(b) it is the acoustic intensity versus

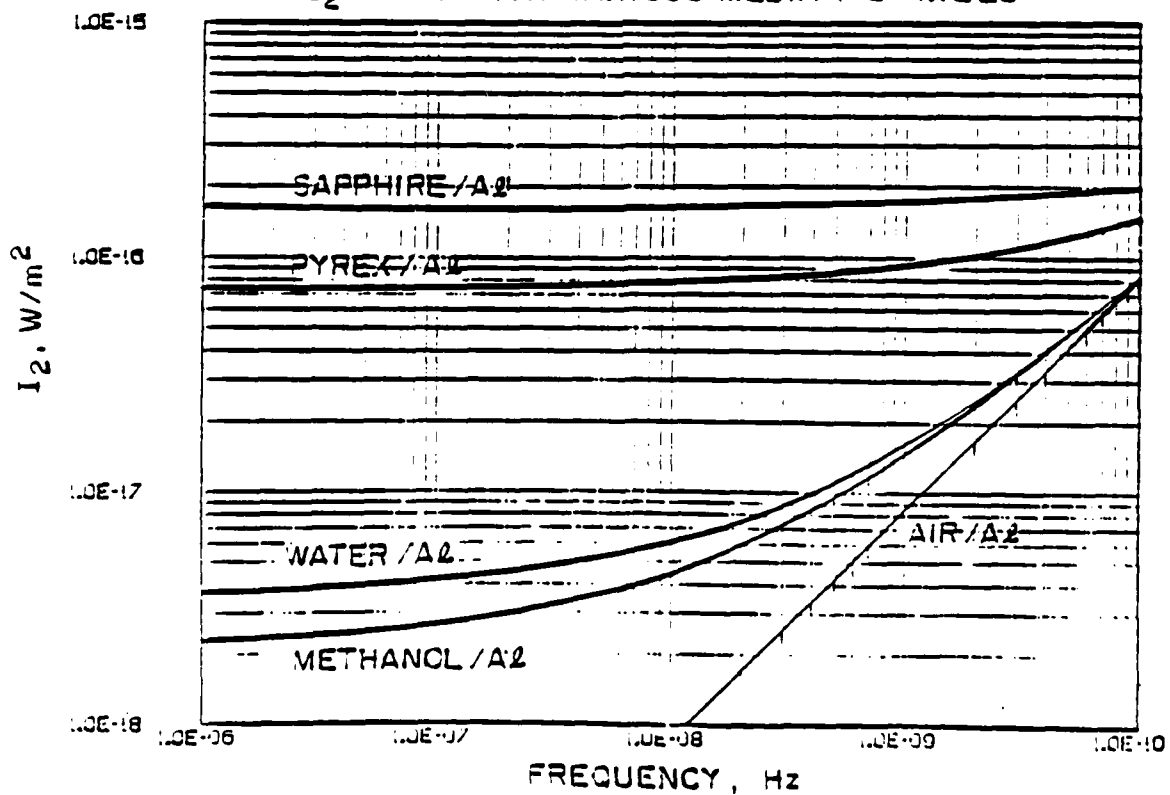
FIG. 5-1

$I_1$  IN VARIOUS MATERIALS WITH  $A_2 \alpha = 1.12 \text{ EB}$



(a)

$I_2$  IN  $A_2$  WITH VARIOUS MEDIA I  $\alpha = 1.12 \text{ EB}$



(b)

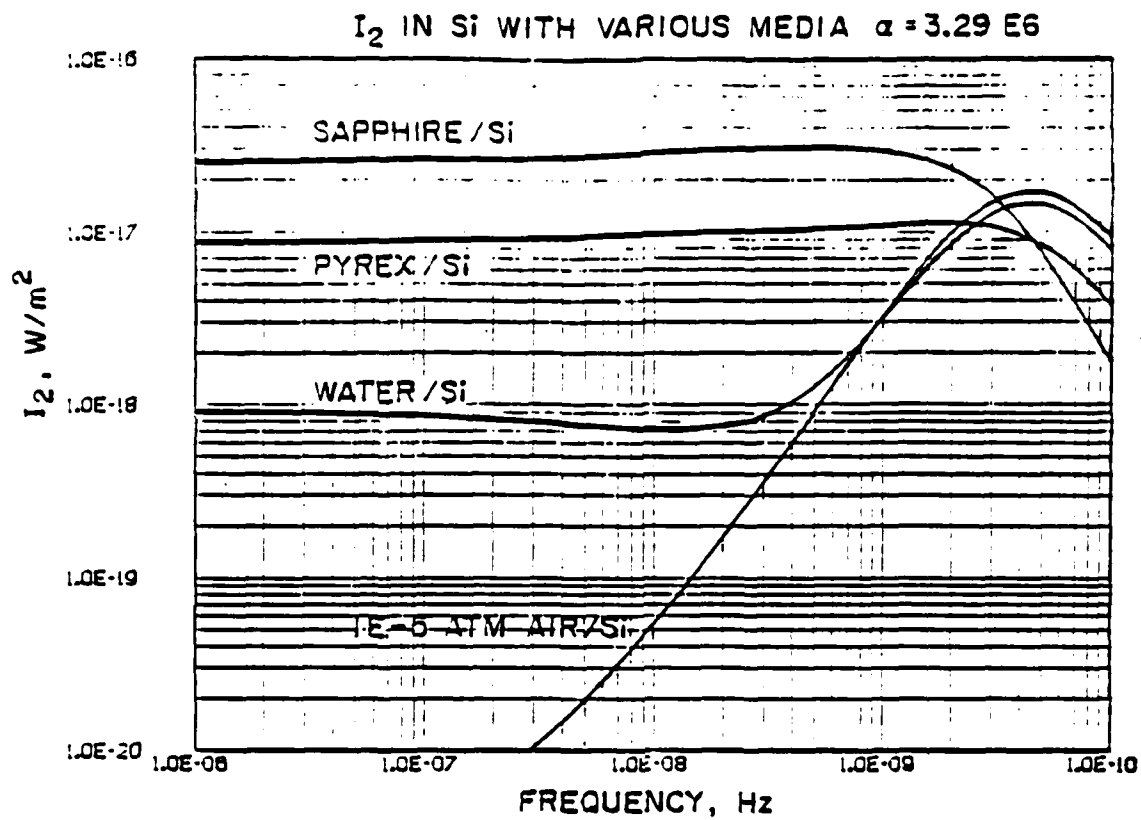


FIGURE 5-10

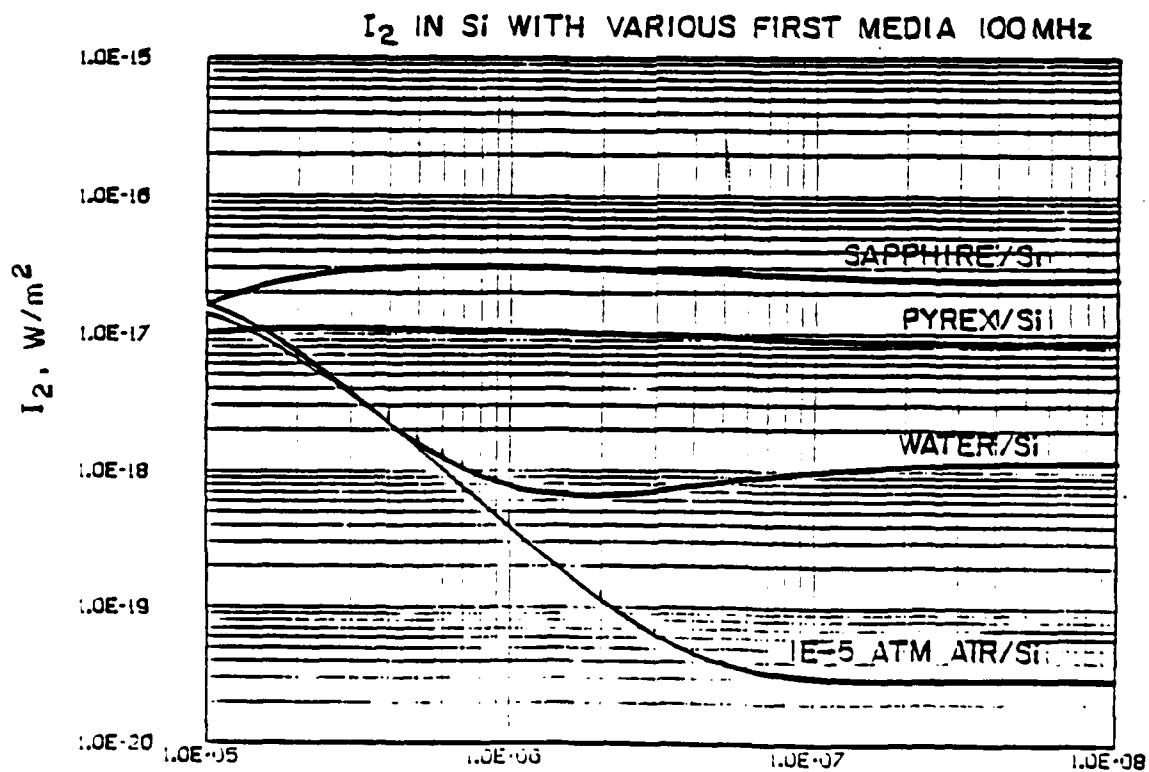


FIG. 5-2

frequency for an optical absorption path that is much longer than used before - typical for silicon. We are aware that the optical absorption length can vary as a function of optical wavelength. We have considered this effect in the plot of Fig. 5-2(b) where we show the optical intensity versus the absorption length. These curves are not that definite when related to an actual sample since we often have more than a single interface. But nonetheless they serve to define the magnitude of the signals that we expect and it allows us to make first estimates on the signal to noise ratios that we might measure in an actual case.

Another way of presenting this information is in the form of the "Intrinsic Conversion Factor." It tells us the sound intensity that is generated at a single interface for  $1 \text{ watt/m}^2$  of absorbed optical power. A table for various materials is shown in Table 5-1. It is to be remembered that the conversion efficiency increases directly as the optical power since the source intensity is proportional to the square of the optical intensity.

TABLE 5-1

Thermal and Acoustic Properties of Selected Materials (20°C unless noted)

Material	Thermal Conductivity K W/m/K	Density $\rho$ kg/m <sup>3</sup>	Capacity C J/kgK	Stiffness $c_{11} = \rho V_s^2$ n/m <sup>2</sup>	Adjusted Linear Coefficient of Thermal Expansion $\beta = \frac{\Delta \rho}{\rho \Delta T}$ K <sup>-1</sup>	Diffusivity $\kappa = K/C$ m <sup>2</sup> /sec	Longitudinal Sound Velocity $V_s$ m/sec	Intrinsic Conversion Factor $\eta = \frac{1}{8} \frac{V_s}{\rho c}$
STP air	.241	1.225	741	.142 E6	.34 E-2	.265 E-3	340	.550 E-8
Acetone	.198	790	2176	.106 E10	.50 E-3	.115 E-6	1158	.96 E-14
Methanol	.155	791	2547	.936 E9	.40 E-3	.769 E-7	1088	.424 E-15
Water	.650	1000	4185	.237 E10	.69 E-4	.155 E-6	1540	.522 E-16
Nitrogen(75 K)	.138	824	1948	.638	.17 E-3	.859 E-7	880	.102 E-14
Pyrex	1.26	2290	975	.730	.27 E-6	.564 E-6	5646	.236 E-19
Sapphire	33	3986	433	.494	.30 E-5	.191 E-4	11130	.168 E-16
Carbon (average)	80	2000	711	.320 E11	.52 E-5	.562 E-4	4000	.133 E-16
Silicon	84	2340	728	.166 E12	.45 E-5	.490 E-4	8415	.171 E-16
Aluminum	300	2699	917	.109 E12	.18 E-4	.121 E-3	6356	.113 E-16
Molybdenum	179	10220	138	.470 E12	.29 E-5	.127 E-3	6780	.170 E-16
Gold	345	19200	130	.189 E12	.13 E-4	.138 E-3	3140	.210 E-15



#### REFERENCES FOR SECTION 5

1. Auld, B.A., Acoustic Fields and Waves in Solids, New York: Wiley, 1973, Chapter 6.

## SECTION 6

### SOME OF THE EXPERIMENTAL RESULTS

The experimental set-up is shown in Fig. 6-1. An Argon Laser modulated at 940 MHz is focused down to a spot on the sample object. The heating within this spot takes place at this frequency and we look for sound at this same frequency. In one instance we hold the sample (a gold film on glass) steady and scan the acoustic lens. In this way we can record a standard acoustic reflection of the image of the heated area. The result is shown in Fig. 6-2. The bright spot is the heated portion of the gold film and the trace below a single A-trace through the image. It is included to show the signal-to-noise ratio.

A photoacoustic image is shown in Fig. 6-3. There we block the acoustic lens and position it so that it is confocal with the optical system. The image is formed by scanning the sample while recording the acoustic signal. The specimen is a patterned gold film on glass. From the optical image in (c) we note the presence of imperfections where the gold film appears to be raised in the form of a small bubble. This striking feature is illustrated in the photoacoustic image of (a). We see there that the raised dots in the gold film appear as black holes. Very little sound is generated. We attribute this to the lack of adhesion between the film and the substrate. This clearly demonstrates one important aspect of photoacoustic imaging — namely — the sensitivity to changes in adhesion of films to the underlying substrates.

In the next two figures we illustrate a second attribute of this form of imaging. The specimen is a layer of silicon on quartz. The silicon is in the form of small crystallites as shown on the left side of Fig. 6-4(a). On the

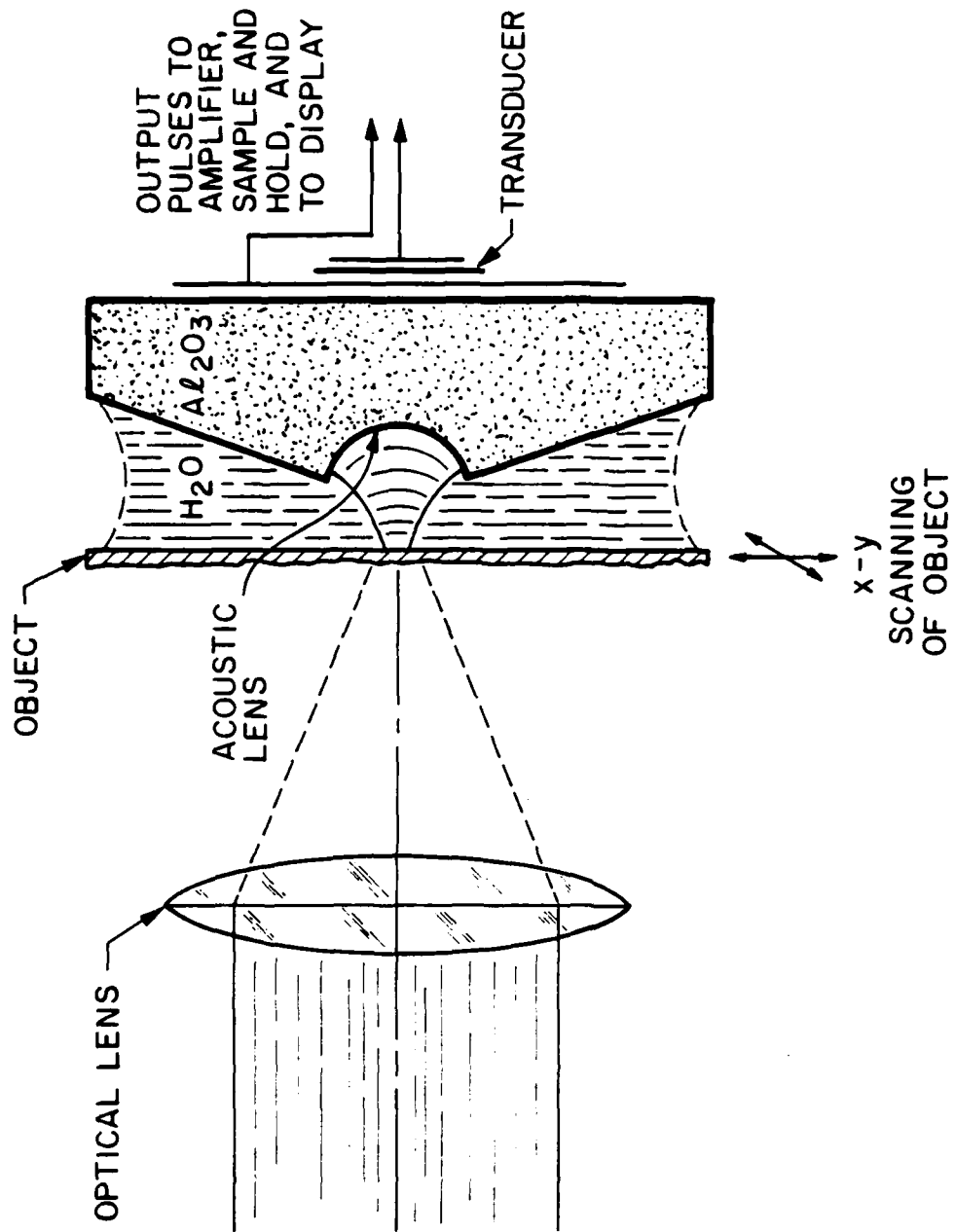
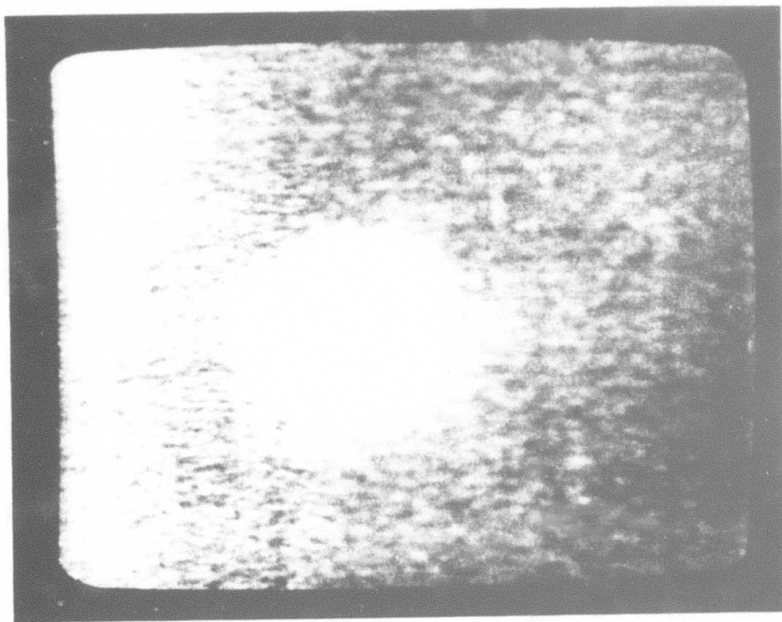
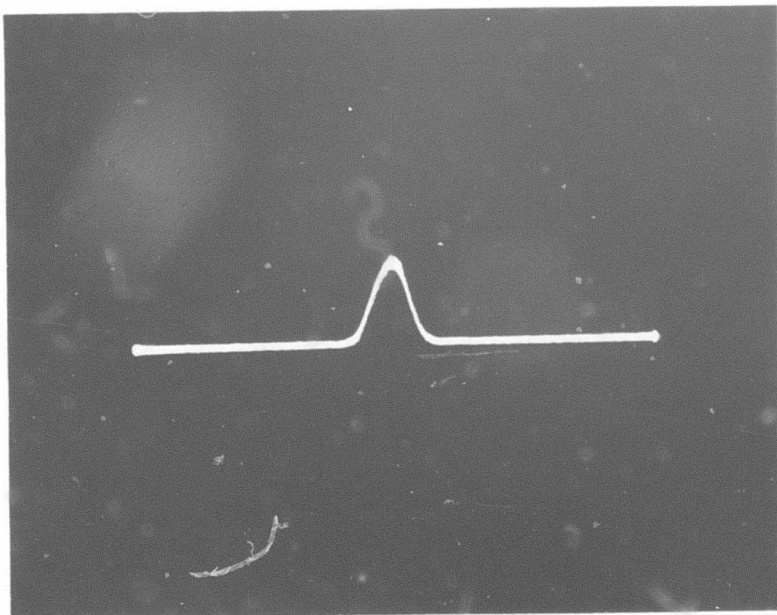


FIGURE 6-1



(a) Acoustic image of thermal spot  
Thermal spot is approximately  $8\mu$  in diameter

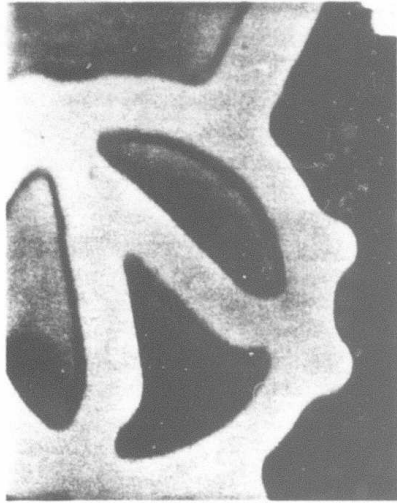


(b) A-trace of one line of the image in (a)

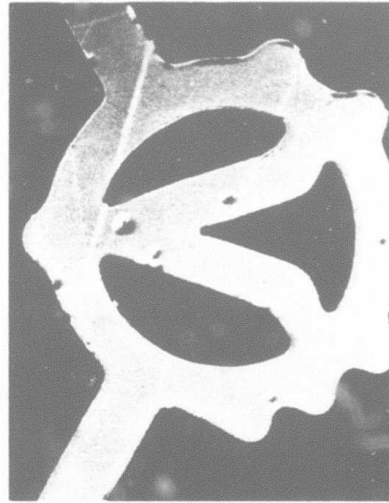
FIGURE 6-2



(a) PHOTOACOUSTIC



(b) ACOUSTIC (IN FOCUS)

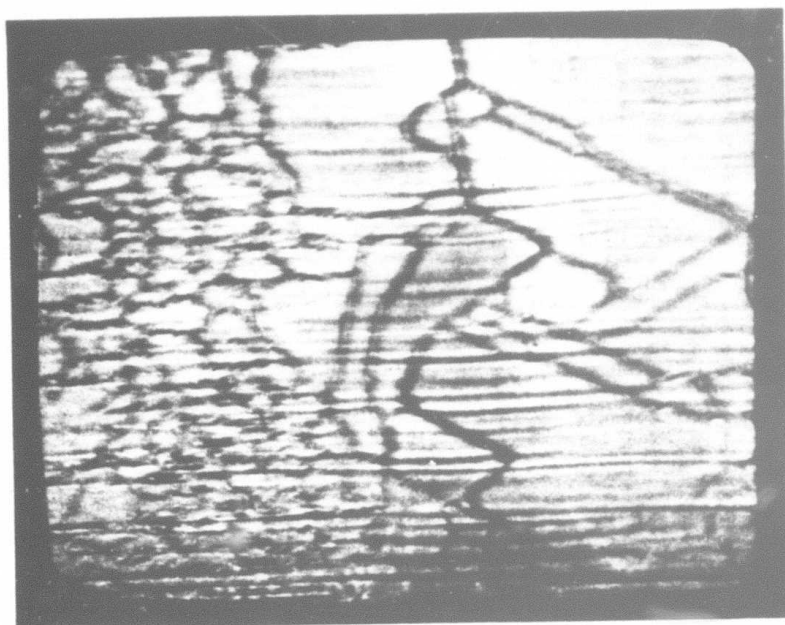


(c) OPTICAL

FIGURE 6-3

right of the figure we see that the crystallites are much larger. The acoustic reflection image of (a) indicates that the reflectivity (acoustic) does not change a great deal as we move across the sample from the region on the left to the region on the right. However, we get a very different result from the sample when we use photoacoustic imaging. There we find the region on the left with the smaller islands is much darker and this we believe is a result of the change in thermal conductivity throughout this area.

Still another aspect is shown in Fig. 6-5. It is a magnified view of the same sample (silicon-on-quartz) in a region that has been laser annealed. The large islands show almost uniform reflectivity in the acoustic reflection image of (a). If we had this image alone we would assume the sample was quite homogeneous - at least within a given island. In a similar manner we would find that the optical image would show a more or less uniform region within the islands. However, in the photoacoustic image of (b) we learn that this sample exhibits a large degree of inhomogeneity. Again we form the conclusion (tentative) that the thermal conductivity of the annealed region shows striking variations. It is only through photoacoustic imaging of this kind that we can observe and monitor this particular property of the material.



(a) Acoustic reflection image (940 MHz)  
(Field of view in (a) and (b) is  $150\mu$ )



(b) Photoacoustic image  
Silicon on quartz - laser annealed

FIGURE 6-4



(a) Acoustic reflection image  
(Field of view in (a) and (b) is  $75\mu$ )



(b) Photoacoustic image  
Annealed silicon layer on quartz

FIGURE 6-5



SECTION 7  
OTHER ITEMS AND SUMMARY

There are other miscellaneous items that have of necessity been covered during the course of this program and they all serve to advance the state of the art for acoustic microscopy.

(1) The advent of the small radii lens which permits us to go to a higher frequency and shorter wavelength requires a much shorter r.f. pulse length since the round trip time in the liquid is only 30 ns. We have succeeded in reducing the pulse length to 8 ns and this has improved the image quality in these small lenses.

(2) We have succeeded with a two frequency version of the microscope wherein we record and store two images each of a different r.f. frequency. We are able to subtract one image from the other and analyze the differences in the two images. It is a good method for displaying those features which are sensitive to the acoustic frequency. We are now planning to expand this system in a way that will enable us to record simultaneous images at multiple frequencies. The "spectrum images" covering a wide range of acoustic frequencies should give us more complete information than has heretofore been possible.

(3) We have built a system for digital recording and storage of the images. The program codes allow for high DMA rates we are now able to store an image consisting of  $512 \times 512 \times 8$  bits onto a floppy disc in less than 20 seconds.

In summary we can state that under this program we have been successful in extending the state of the art. We now find that other laboratories have found this system attractive to the point where they have constructed

their own instruments. At General Electric in Schenectady, Dr. Gilmore has built a computer controlled microscope that is used for the purpose of characterizing materials ranging from steels to solar cells. At IBM in Yorktown, Dr. Hollis has built an instrument for studying the properties of materials and fabricated devices. At Bell Labs in Murray Hill, Dr. Bishop is building an instrument also to be used for material characterization. And at Hughes Aircraft in Culver City, Dr. Zelick is developing an instrument that is to be used on the VHSIC program. All of these are designed in conformity with the principles that were conceived during the course of this contract.

Abroad we find that two firms have announced plans for producing commercial versions of the acoustic microscope - Heit Optical Company in Wetzlar, West Germany and Olympics Optical Company in Tokyo, Japan. With the entry of these two companies we will have instruments available in a large number of laboratories. We believe that this technology which provides us with a new and improved method for viewing the microscopic world is well established and it will become a standard tool for investigation and characterization in the material world.

## PUBLICATIONS

1. A. Atalar, V. Jipson and C.F. Quate, "Acoustic Microscopy for Materials Characterization," Proceedings of the ARPA/AFML Review of Progress in Quantitative NDE, July 17-21, 1978, La Jolla, California, AFML-TR-78-205, pp. 252-256.
2. R.A. Lemons and C.F. Quate, "Acoustic Microscopy," in Physical Acoustics, W.P. Mason and R.N. Thurston, Eds. (Academic Press, New York, 1979), Vol. XIV, pp. 2-92.
3. H.K. Wickramasinghe, R.C. Bray, V. Jipson, C.F. Quate and J.R. Salcedo, "Photoacoustics on a Microscopic Scale," Ginzton Laboratory Report No. 2850, Stanford University (August 1978); Appl. Phys. Lett. 33, 9239-925.
4. C.F. Quate, "Ultrasonic Imaging," Ginzton Laboratory Report No. 2882, Stanford University (November 1978); in Electronics Imaging, The Rank Prize Funds Opto-Electronics Biennial Symposia, T.P. McLean and P. Schagen, Editors, Academic Press, Inc. (London) Ltd., 365-393, 1979.
5. A. Atalar, V. Jipson, R. Koch and C.F. Quate, "Acoustic Microscopy with Microwave Frequencies," Ginzton Laboratory Report No. 2884, Stanford University (November 1979); in Annual Review of Materials Science, Vol. 9, 255-281 (August 1979).
6. C.F. Quate, A. Atalar and H.K. Wickramasinghe, "Acoustic Microscopy with Mechanical Scanning - A Review," Ginzton Laboratory Report No. 2911, Stanford University (January 1979); Proceedings, IEEE, 67, 1092-1114 (August 1979).
7. C.F. Quate, "Acoustic Microscopy," Ginzton Laboratory Report No. 2989, Stanford University (July 1979); Scientific American, 241, 58-66, (October 1979).
8. C.F. Quate, "A Comparison of Acoustic Microscopy, Imaging, Holographic and Tomographic Procedures," ARPA/AFML Review of Progress in Quantitative NDE, July 8-13, 1979, La Jolla, California.
9. A. Atalar and C.F. Quate, "Acoustic Microscopy via Scanning," ARPA/AFML Review of Progress in Quantitative NDE, July 8-13, 1979, LaJolla, California (poster session).
10. C.F. Quate, "Microscope, Acoustic," McGraw-Hill Encyclopedia of Science and Technology, 5th Edition (in press).

11. R.C. Bray and C.F. Quate, "Recent Progress in Materials Studies with Acoustic Microscopy," Conference Proceedings, ARPA/AFML Review of Progress in Quantitative NDE, July 1980.
12. R.C. Bray, J. Calhoun, R. Koch and C.F. Quate, "Film Adhesion Studies with the Acoustic Microscope, Journal of Thin Solid Films, 74, 295-302 (1980).
13. C.F. Quate, "Microwaves, Acoustics and Scanning Microscopy," Ginzton Laboratory Report No. 3175, Stanford University (September 1980); in Proceedings of the Rank Prize International Symposium on Scanned Image Microscopy, E.A. Ash, ed., Academic Press (1980).